

A crustal source for ca. 165 Ma post-collisional granites related to mineralization in the Jianglang dome of the Songpan-Ganzi Orogen, eastern Tibetan Plateau

Yanpei Dai^a, Yudi Zhu^{b,*}, Tongzhu Li^a, Huihua Zhang^a, Gaolin Tang^c, Zhanwu Shen^a

^a Chengdu Center, China Geological Survey, Chengdu 610081, PR China

^b School of Geoscience and Technology, Southwest Petroleum University, Chengdu 610500, PR China

^c Sichuan Liwu Copper Mining Company, Kangding 626200, PR China

ARTICLE INFO

Keywords:

Zircon U-Pb-Hf isotopes
I-type granites
Post-collisional extension
Crustal melts
Songpan-Ganzi Orogen

ABSTRACT

The Wenjiaping and Wulaxi granite plutons are located in the Jianglang dome, which is a key domain for providing deep insight into the tectonic evolution of the Songpan-Ganzi Orogen. Two granites are composed chiefly of K-feldspar, quartz, biotite with minor plagioclase and hornblende. This study presents zircon U-Pb chronology, geochemistry and Hf isotope data to explore their petrogenesis and metallogenetic implications. Zircon U-Pb dating provides crystallization ages of 164.5 ± 0.9 Ma and 163.4 ± 0.9 Ma for the Wenjiaping granite, and 164.3 ± 1.7 Ma for the Wulaxi granite. This indicates that they were formed synchronously. They also contain inherited zircons related to the Rodinia and Gondwana supercontinents and the Emeishan large igneous province. Their mineral assemblages lack peraluminous (e.g., garnet and cordierite) and high-temperature (e.g., pyroxene and fayalite) minerals. They are characterized by low A/CNK (1.10–0.99), FeO^T/MgO (8.55–2.83) and $\text{K}_2\text{O}/\text{N}_2\text{O}$ ratios (1.34–0.51) with low $\text{Zr} + \text{Nb} + \text{Ce} + \text{Y}$ concentrations (average 258 ppm) and zircon saturation temperatures (781–651 °C). Their Al_2O_3 , P_2O_5 and SiO_2 contents show negative correlations, and they thus fit the I-type granite definition. Some major and trace elements exhibit strong correlations, implying extensive fractional crystallization (e.g., hornblende and ilmenite) during the magma evolution. Two granites show enrichment in light rare earth elements and large ion lithophile elements, and depletion in high field strength elements. They have low $\text{Mg}^{\#}$ values (38.7–17.3) and Y/Nb ratios (0.45–0.16), and yield dominantly negative $\varepsilon_{\text{Hf}}(t)$ values (1.4––13.9), indicating a heterogeneous source and their derivation from remelting of ancient continental crust (e.g., Mesoproterozoic Liwu Group in this region) with minor juvenile crust. Combined with prior studies, we conclude that the Wenjiaping and Wulaxi granites were formed in a post-collisional extensional regime, and were responsible for the 163.7–151.1 Ma magmatic hydrothermal Cu-W mineralization in the Jianglang dome. In addition, two granite plutons intrude this dome and they are undeformed, implying that the doming was during the Early to Middle Jurassic.

1. Introduction

The Songpan-Ganzi Orogen (SGO) is located in the eastern part of the Tibetan Plateau and to the west of the Yangtze Block. It was formed during final closure of the Paleo-Tethys Ocean and Triassic continental collision between the North China, Yangtze and Qiangtang Blocks (Xu et al., 1992). The SGO is characterized by a thick (5–15 km) Triassic flysch sequence that was extensively intruded by Late Triassic to Early Jurassic granites (Roger et al., 2010). Previous studies on petrogenesis of Triassic flysch and syn- to late-collisional granites (220–200 Ma, Roger et al., 2010) have been carried out. Based on U-Pb chronological study of 870 detrital zircon grains from the Triassic sediments, their

provenance includes the Qinling-Dabie Orogen, North China Block and Yangtze Block (Weislogel et al., 2006). The Triassic orogeny involves shortening and subsequent crustal thickening of the orogenic wedge, which induced the emplacement of syn- to late-collisional granites (Roger et al., 2004, 2010). However, little attention has been paid to post-collisional magmatism (200–150 Ma, Roger et al., 2010), which may offer geodynamic information on tectonic evolution and lithospheric extension of the SGO (Zhang et al., 2007).

Several extensional tectonic domes were identified in the eastern margin of the SGO. They were classified as metamorphic core complexes, and can help us to understand geological evolution of the eastern Tibetan Plateau (Yan et al., 1997, 2003; Zhou et al., 2002). The Jianglang dome

* Corresponding author.

E-mail address: 289312722@qq.com (Y. Zhu).

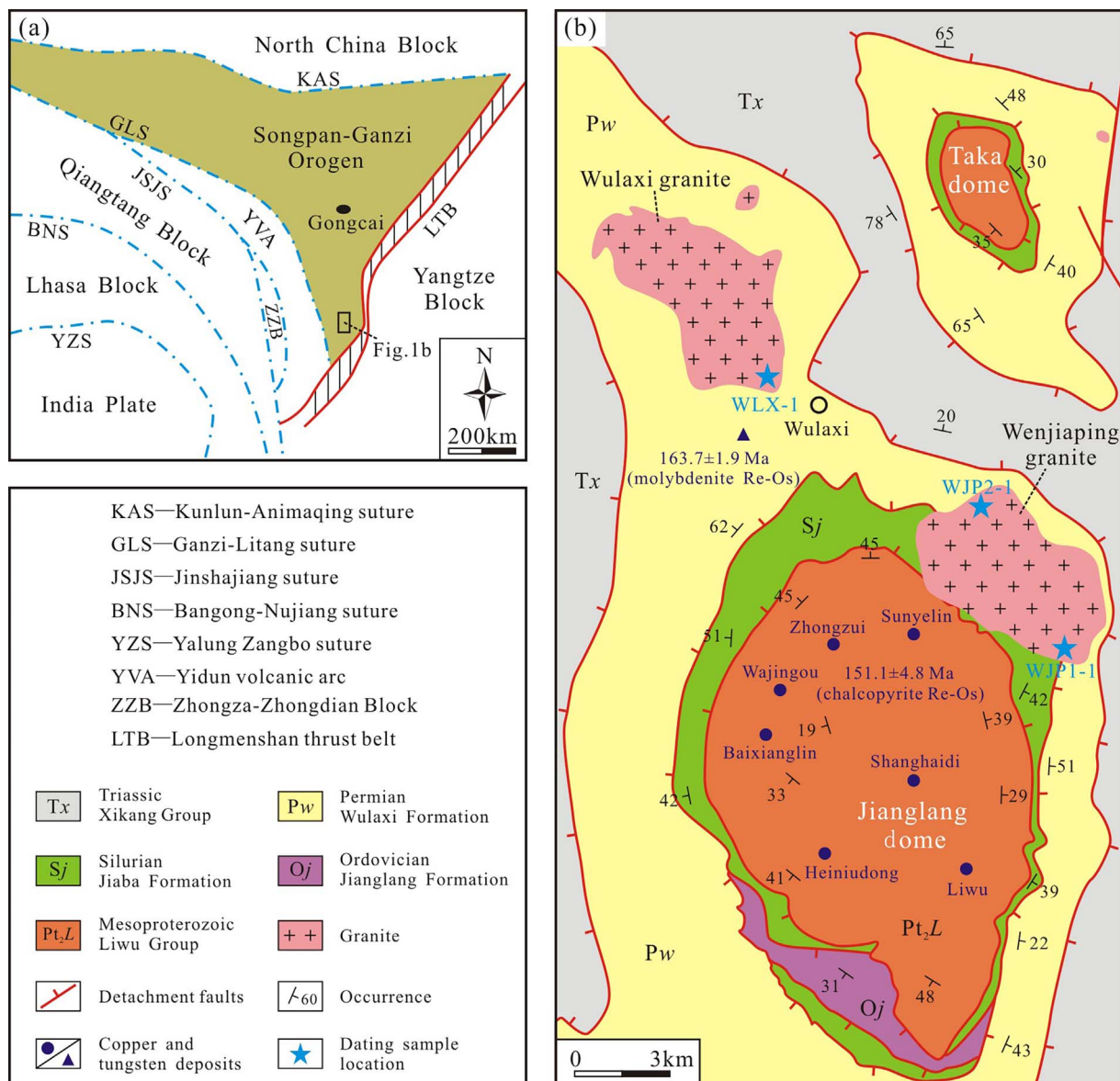


Fig. 1. Tectonic position (a) and geological map (b) of the Jianglang dome, modified after Yan et al. (2003).

situates in the southern rim of the SGO. A series of hydrothermal high-grade (average 2.5 wt.% Cu, Dai et al., 2016) Cu-sulfide deposits occur in its core (Fig. 1). Previous sulfur and boron isotopic systematics indicated a magmatic hydrothermal affinity with granite plutons in the north of the Jianglang dome (Chen et al., 2011; Zhou et al., 2017). However, robust chronological constraints are lacking, and the granite petrogenesis remains an enigma. In the present study, we performed major and trace elements, LA-ICP-MS zircon U-Pb dating, and Hf isotope to explore petrogenesis and metallogenetic implications of the Wenjiaping and Wulaxi granites. These data indicate that they are I-type granites that were emplaced at ca. 164.5–163.4 Ma with dominantly negative $\epsilon_{\text{Hf}}(t)$ values (1.4 to –13.9). When combined with prior studies in this region, our determinations strongly support a heterogeneous derivation from remelting of ancient continental crust with minor juvenile crust for the investigated post-collisional granites, and a magmatic hydrothermal affinity for the Cu-W deposits in the Jianglang dome.

2. Geological background and granite petrography

The SGO covers a triangular-shaped area of about $2.2 \times 10^5 \text{ km}^2$ at the junction of the North China, Yangtze and Qiangtang Blocks. This

region is bounded by the Longmenshan thrust belt to the east, Kunlun-Animaqing suture to the north, and Jinshajiang suture and Yidun volcanic arc to the southwest (Xu et al., 1992). The SGO is mainly filled by a 5–15 km thick succession of Middle to Late Triassic flysch named Xikang Group, and a 4–6 km thick pre-Triassic strata exposed along its eastern and southern margins (Roger et al., 2010). The voluminous flysch series are dominated by a sequence of alternating shale and sandstone, with minor carbonate and greywacke. They were fed from a peripheral arc and the adjacent continental blocks, and also recorded supracrustal history during the Triassic continental collision (Weislogel et al., 2006). During the Late Triassic, the flysch complex was intensely deformed by folding and thrusting, which clearly indicate a compressional tectonic regime (Harrowfield and Wilson, 2005). At that time, granitoid melts intruded the flysch series, with Sr-Nd-Pb isotopic compositions showing a derivation from melting of the Proterozoic basement and negligible mantle source contribution (Roger et al., 2010). However, the Late Triassic granite intrusions commonly have A-type and adakitic affinities, and were indicative of delamination-related extension (Roger et al., 2004; Xiao et al., 2007; Zhang et al., 2007). These contradictory interpretations imply the variable responses of different lithospheric levels to the collisional event (Yuan et al., 2010).

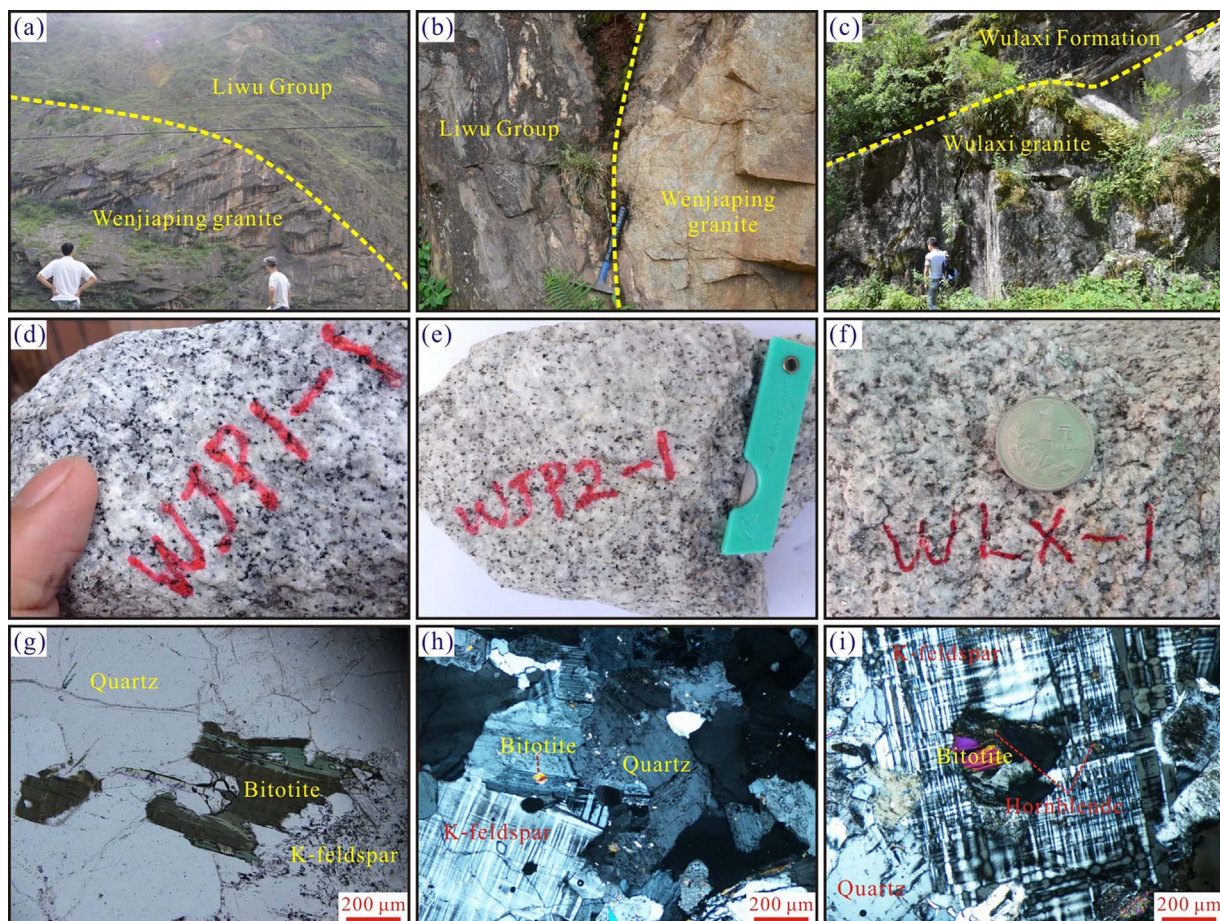


Fig. 2. Field and microscopic features of the studied granites. (a-b) The Wenjiaping pluton intrudes the Liwu Group. (c) The Wulaxi granite pluton intrudes the Wulaxi Formation. (d-f) Dated samples of the Wenjiaping and Wulaxi granites. (g-i) Mineral assemblages of the Wenjiaping and Wulaxi granites.

The Jianglang dome is located in the southern margin of the SGO (Fig. 1a). They consist of three tectonostratigraphic units, including: (1) a core of schist complex known as the Mesoproterozoic Liwu Group; (2) an overlying ductilely deformed middle slab of the Paleozoic metasedimentary and metabasic rocks; and (3) a weakly metamorphosed sedimentary cover of the Triassic Xikang Group (Yan et al., 2003). The Liwu Group mainly comprises two-mica (\pm quartz) schist, quartzite and minor interlayered metabasalt. The metabasalt interlayers have whole rock Sm-Nd isochron age of 1677–1674 Ma (Yan et al., 1997). The middle slab is chiefly composed of: (1) the Ordovician Jianglang Formation of quartzite and phyllite; (2) the Silurian Jiaba Formation of metasilicalite, carbonaceous slate and minor metabasalt; and (3) the Permian Wulaxi Formation of marble with sandwiched metabasalt (SBGMR, 1991). This unit is separated from both the upper cover unit and the lower core complex by detachment faults, and numerous extensional faults occur in the middle slab (Yan et al., 1997, 2003).

In recent decades, several Cu-sulfide deposits have been found within the Liwu Group, including Liwu, Heiniudong, Zhongzui, Wajingou and Baixianglin (Fig. 1b). They contain an average Cu grade of 2.5 wt.% and total Cu reserve of more than 0.8×10^6 tons (Feng et al., 2008; Dai et al., 2016). Their orebodies are stratiform with occurrences parallel to the wallrock foliation planes. The sulfide ores show massive, banded, veined and disseminated structures. Their main ore minerals are pyrrhotite and chalcopyrite with minor sphalerite, galena and pyrite. All the orebodies occur in the alteration zones which are widely distributed in the deposit areas, suggesting a hydrothermal origin for the Cu mineralization (Yan et al., 1997; Chen et al., 2011; Zhou et al., 2017). The major alteration types are silicification, biotitization, sericitization, chloritization, garnetization and tourmalinization. Fluid inclusion studies have uncovered

that the ore fluids are characterized by moderate to low temperatures (344–131 °C), low salinity (average 15.67 wt%NaCl.eqv) and CO₂-rich (Feng et al., 2008). Prior sulfur isotopic data of metal sulfides ($\delta^{34}\text{S} = 7.5\text{--}1.5\text{\textperthousand}$) and boron isotopic data of ore-associated tourmalines ($\delta^{11}\text{B} = -15.47 \pm 0.83\text{\textperthousand}$ to $-5.91 \pm 0.67\text{\textperthousand}$) indicated a magmatic hydrothermal affinity (Yan et al., 1997; Chen et al., 2011; Zhou et al., 2017). Recently, Zhou et al. (2017) obtained a chalcopyrite Re-Os isochron age of 151.1 ± 4.8 Ma ($n = 5$, MSWD = 5.8) for the Liwu and Zhongzui Cu-sulfide deposits.

The investigated Wenjiaping and Wulaxi granite plutons are distributed in the north of the Jianglang dome. They occupy outcrop areas of $\sim 34 \text{ km}^2$ and $\sim 32 \text{ km}^2$, respectively (Fig. 1b). To the south of the Wulaxi pluton, several skarn tungsten deposits are developed within the Permian Wulaxi Formation. Molybdenite Re-Os dating indicates an isochron age of 163.7 ± 1.9 Ma ($n = 6$, MSWD = 0.42) for them (Li et al., 2016). In the field, two granite plutons intrude the Liwu Group and the Wulaxi Formation, respectively (Fig. 2a–c). Our dated samples are shown in Fig. 2d–f. Their locations are marked in Fig. 1b. Two plutons commonly exhibit porphyritic texture and massive structure in hand specimens, and they show uniform lithologic features on thin sections (Fig. 2g–i). The phenocrysts are primarily composed of K-feldspar (~20%) and minor plagioclase (~2%). The K-feldspar grains are large in size (2.5–1.0 mm). They are euhedral to subhedral with apparent crossed twins. In some locations, they enclose biotite and hornblende grains (Fig. 2h–i). The platy plagioclase phenocrysts are subhedral (1.3–0.8 mm) with polysynthetic twins. The groundmass forms ~80% of the granites, and mainly consists of subhedral to anhedral quartz (~35%), K-feldspar (~25%), biotite (~10%), plagioclase (~3%) and hornblende (< 3%). These medium- to fine-grained

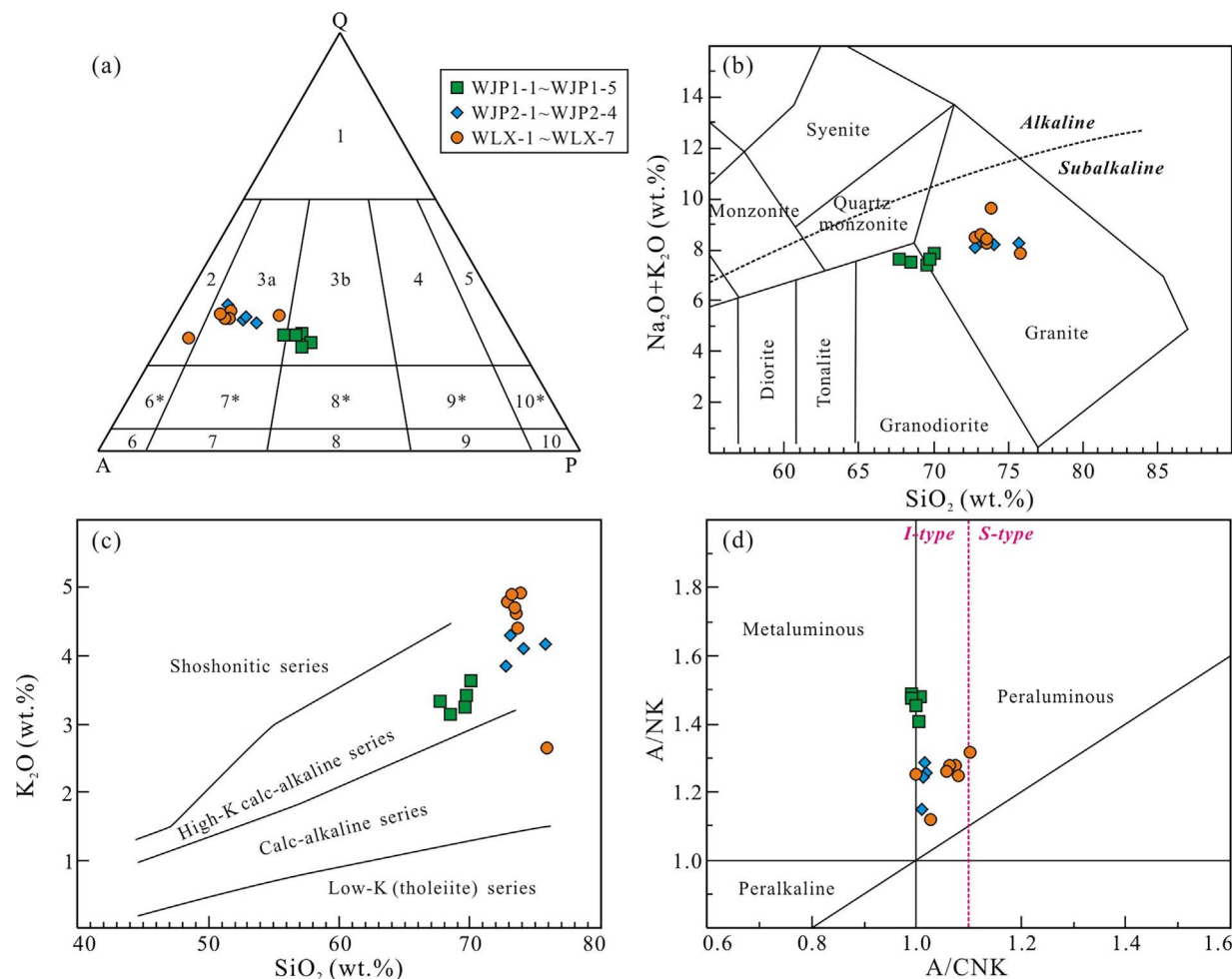


Fig. 3. (a) Quartz-alkali feldspar-plagioclase (QAP) diagram (Le Maitre, 1989), 1 = quartzolite, 2 = alkali feldspar granite, 3a = syenogranite, 3b = monzogranite, 4 = granodiorite, 5 = tonalite, 6* = quartz-alkali feldspar syenite, 7* = quartz syenite, 8* = quartz monzonite, 9* = quartz monzodiorite/quartz monzogabbro, 10* = quartz diorite/quartz gabbro/quartz anorthosite, 6 = alkali feldspar syenite, 7 = syenite, 8 = monzonite, 9 = monzodiorite/monzogabbro, 10 = diorite/gabbro/anorthosite. (b) Total alkali vs. silica (TAS) diagram (Middlemost, 1994), with the dashed line from Irvine and Baragar (1971). (c) K₂O vs. SiO₂ diagram (Peccerillo and Taylor, 1976). (d) The molar Al₂O₃/(Na₂O + K₂O) vs. Al₂O₃/(CaO + Na₂O + K₂O) diagram (A/NK vs. A/CNK, Maniar and Piccoli, 1989).

minerals are mostly 0.5–0.05 mm in size. The quartz grains show wavy extinction in some cases. The accessory minerals mainly include magnetite (< 2%) and zircon (< 1%). According to the CIPW normative mineral calculation, the granite samples are dominantly plotted in the field of syenogranite and monzogranite on the quartz-alkali feldspar-plagioclase (QAP) diagram (Fig. 3a). This is consistent with our field and microscopic observations.

3. Analytical methods

Sixteen granite samples were crushed to 200 mesh for major and trace element analyses. Samples WJP1-1, WJP2-1 and WLX-1 (Fig. 2d-f) were chosen for zircon U-Pb and Hf isotopic measurements. Major and trace elements analyses were performed in the Analytical Laboratory of ALS Chemex (Guangzhou) Company Limited. Detailed procedures are given by Sun et al. (2016). Major oxides measurements were conducted using a PANalytical Axios-advance (Axios PW4400) X-ray fluorescence spectrometer. Analytical precision was less than 5% as determined for the National Standards STSD-4 and SY-4. Loss on ignition (LOI) was obtained using 3 g of powder heated to 1100 °C for one hour. Trace elements measurements were performed using a Perkin-Elmer Elan 9000 ICP-MS. Analyses of the international standards OREAS-104 and SY-4 indicated a precision generally better than 10% for all trace elements.

Zircons were separated with conventional heavy liquid and

magnetic separation methods. The grains were mounted in epoxy, polished and then gold-coated. Cathodoluminescence (CL) images were taken to examine their internal morphology. Zircon U-Th-Pb isotopic measurements were conducted at Nanjing FocuMS Technology Co. Ltd. Teledyne Cetac Technologies Analyte Excite laser-ablation system (Bozeman, Montana, USA) and Agilent Technologies 7700 x quadrupole ICP-MS (Hachioji, Tokyo, Japan) were combined for zircon U-Pb dating. The 193 nm ArF excimer laser, homogenized by a set of beam delivery systems, was focused on zircon surface with fluence of 6.0 J/cm². Ablation protocol employed a spot diameter of 35 μm at 8 Hz repetition rate for 40 s (equating to 320 pulses). Helium was applied as carrier gas to efficiently transport aerosol to ICP-MS. Zircon 91500 was used as an external standard to correct instrumental mass discrimination and elemental fractionation during the ablation. Zircon GJ-1 was treated as quality control for geochronology. These two standards were analyzed every eight analyses. The obtained mean ²⁰⁷Pb/²⁰⁶Pb age of 91500 (1063.2 ± 1.8 Ma) and ²⁰⁶Pb/²³⁸U age of GJ-1 (600.4 ± 2.5 Ma) are within experimental error of their recommended values (1065.4 ± 0.6 Ma, Wiedenbeck et al., 1995; 599.8 ± 4.5 Ma, Jackson et al., 2004). Lead abundance of zircon was external calibrated against NIST SRM 610 with Si as internal standard. Raw data reduction was performed off-line by ICPMSDataCal software (Liu et al., 2010).

In situ zircon Hf isotopic measurements were conducted at Nanjing FocuMS Technology Co. Ltd. The analyses were performed on the same zircon grains previously analyzed for U-Pb dating. Teledyne Cetac

Table 1

Major (wt.%) and trace element (ppm) contents of the Wenjiaping and Wulaxi granite samples.

Samples	WJP1-1	WJP1-2	WJP1-3	WJP1-4	WJP1-5	WJP2-1	WJP2-2	WJP2-3	WJP2-4	WLX-1	WLX-2	WLX-3	WLX-4	WLX-5	WLX-6	WLX-7
Granites	The Wenjiaping granite															The Wulaxi granite
SiO ₂	70.09	69.57	68.46	67.70	69.73	73.08	74.08	72.78	75.73	73.56	73.91	75.82	72.80	73.36	73.17	73.59
TiO ₂	0.31	0.38	0.42	0.45	0.34	0.12	0.10	0.15	0.06	0.16	0.02	0.02	0.15	0.17	0.17	0.10
Al ₂ O ₃	15.26	15.38	15.75	15.70	15.40	14.05	13.96	14.36	12.90	14.46	14.66	14.30	14.42	14.46	14.32	14.24
Fe ₂ O ₃ ^T	2.13	2.58	2.68	3.02	2.30	1.21	1.01	1.19	0.86	1.21	0.57	0.19	1.19	1.23	1.37	1.02
MnO	0.04	0.04	0.05	0.05	0.04	0.04	0.03	0.05	0.02	0.02	0.12	0.01	0.02	0.02	0.04	0.06
MgO	0.60	0.78	0.85	0.96	0.71	0.22	0.18	0.30	0.12	0.25	0.06	0.06	0.24	0.25	0.27	0.15
CaO	2.37	2.67	2.92	2.85	2.65	1.42	1.40	1.62	0.85	1.18	0.64	1.58	1.16	1.26	1.20	0.98
Na ₂ O	4.21	4.18	4.36	4.27	4.18	3.97	4.11	4.25	4.07	3.62	4.73	5.21	3.71	3.78	3.67	4.03
K ₂ O	3.63	3.25	3.14	3.34	3.43	4.30	4.11	3.86	4.17	4.63	4.92	2.65	4.80	4.71	4.91	4.40
P ₂ O ₅	0.10	0.13	0.14	0.16	0.12	0.04	0.04	0.05	0.01	0.09	0.13	0.10	0.08	0.09	0.11	0.12
LOI	0.96	0.32	0.41	0.37	0.38	0.80	0.33	0.50	0.20	0.68	0.31	0.38	0.71	0.53	0.58	1.43
Total	99.70	99.28	99.18	98.87	99.28	99.35	99.35	99.11	98.99	99.86	100.07	100.32	99.28	99.86	99.81	100.12
A/NK	1.41	1.48	1.49	1.48	1.45	1.26	1.25	1.29	1.15	1.32	1.12	1.25	1.28	1.28	1.26	1.25
A/CNK	1.01	1.01	0.99	0.99	1.00	1.02	1.01	1.02	1.01	1.10	1.03	1.00	1.08	1.06	1.06	1.08
FeO ^T /MgO	3.19	2.98	2.84	2.83	2.91	4.95	5.05	3.57	6.45	4.36	8.55	2.85	4.46	4.43	4.57	6.12
Na ₂ O + K ₂ O	7.84	7.43	7.50	7.61	7.61	8.27	8.22	8.11	8.24	8.25	9.65	7.86	8.51	8.49	8.58	8.43
K ₂ O/Na ₂ O	0.86	0.78	0.72	0.78	0.82	1.08	1.00	0.91	1.02	1.28	1.04	0.51	1.29	1.25	1.34	1.09
Mg [#]	35.9	37.5	38.6	38.7	38.0	26.5	26.1	33.4	21.7	29.1	17.3	38.5	28.6	28.7	28.1	22.6
La	62.4	76.6	83.9	83.5	60.8	24.5	30.0	30.4	7.50	39.0	4.50	4.70	40.0	40.5	52.1	27.6
Ce	106	128	141	143	104	41.9	53.2	52.2	14.8	69.8	8.20	8.70	69.6	70.4	87.6	47.5
Pr	8.78	11.0	12.6	12.0	8.91	3.76	4.77	4.66	1.42	6.62	0.77	0.80	6.96	7.09	8.79	4.87
Nd	29.6	36.4	42.0	40.8	29.9	12.4	15.5	15.5	5.00	22.9	2.20	2.30	22.1	23.8	27.1	15.5
Sm	4.14	4.89	5.75	5.49	4.16	1.77	2.31	2.42	0.97	4.41	0.71	0.63	4.11	4.14	4.71	2.88
Eu	1.21	1.32	1.53	1.41	1.15	0.57	0.60	0.67	0.23	0.62	0.05	0.11	0.64	0.66	0.71	0.48
Gd	3.09	3.52	4.16	3.98	3.01	1.29	1.63	1.72	1.03	2.68	0.63	0.67	2.49	2.42	2.81	2.62
Tb	0.36	0.39	0.51	0.44	0.35	0.19	0.22	0.23	0.17	0.40	0.20	0.17	0.38	0.39	0.46	0.43
Dy	2.09	2.12	2.63	2.52	2.00	1.09	1.27	1.25	1.06	2.16	1.30	0.95	1.89	1.82	1.97	2.63
Ho	0.37	0.38	0.47	0.44	0.35	0.24	0.26	0.25	0.23	0.37	0.24	0.18	0.32	0.36	0.36	0.45
Er	0.99	0.99	1.22	1.14	0.89	0.69	0.80	0.71	0.76	0.84	0.69	0.45	0.95	0.91	0.90	1.21
Tm	0.15	0.14	0.17	0.16	0.12	0.11	0.13	0.11	0.13	0.10	0.07	0.07	0.12	0.12	0.13	0.19
Yb	0.94	0.88	1.07	0.95	0.71	0.79	0.93	0.76	0.99	0.82	0.75	0.47	0.71	0.68	0.75	1.09
Lu	0.14	0.13	0.16	0.15	0.11	0.14	0.16	0.13	0.18	0.14	0.11	0.07	0.11	0.11	0.12	0.16
ΣREE	220	266	297	296	216	89.4	112	111	34.5	151	20.5	20.3	150	153	189	108
(La/Yb) _N	44.9	58.8	53.0	59.4	57.9	21.0	21.8	27.0	5.12	32.1	4.05	6.76	38.1	40.2	46.9	17.1
Yb _N	3.79	3.55	4.31	3.83	2.86	3.19	3.75	3.06	3.99	3.31	3.02	1.90	2.86	2.74	3.02	4.40
Eu/Eu [*]	0.99	0.93	0.91	0.88	0.95	1.10	0.90	0.96	0.70	0.51	0.22	0.51	0.57	0.59	0.55	0.52
Rb	159	140	140	167	145	229	216	225	285	264	296	139	251	244	235	306
Sr	729	704	716	698	702	357	314	391	71.4	243	38.3	108	241	258	256	164
Ba	1405	1580	1530	1395	1540	707	510	615	66.3	783	37.7	141	819	858	991	462
Nb	26.4	26.8	29.8	31.1	23.7	27.1	25.7	32.5	45.9	26.1	52.7	40.6	24.6	21.7	29.2	41.7
Ta	1.70	1.50	1.80	1.70	1.40	1.50	1.80	1.70	4.20	2.70	6.40	5.90	2.00	1.60	2.10	2.90
Zr	226	271	276	289	225	127	124	135	61.0	105	29.0	23.0	105	111	126	72.0
Hf	5.20	5.40	5.90	6.10	4.70	3.70	4.00	3.60	2.80	3.30	1.70	0.90	2.90	3.00	3.30	2.10
Th	23.2	25.2	29.5	28.5	21.0	19.7	32.0	18.8	22.1	19.9	3.01	3.30	19.5	20.2	24.0	13.5
U	7.79	3.48	4.28	4.30	3.51	10.3	10.3	5.81	30.4	10.9	24.6	15.2	6.72	9.60	3.20	20.0
Cs	5.41	4.88	5.08	6.34	4.42	5.68	4.97	5.66	2.26	9.18	3.97	2.66	8.56	13.1	6.84	8.47
Ga	22.3	21.0	21.7	23.6	21.2	22.0	22.8	23.1	25.1	22.1	25.0	25.0	22.7	22.1	20.9	24.5
Y	11.0	11.4	13.0	13.1	10.3	7.90	8.60	8.50	8.90	11.4	9.70	6.30	10.2	9.80	10.4	15.0
10000 × Ga/Al	2.76	2.58	2.60	2.84	2.60	2.96	3.09	3.04	3.68	2.89	3.22	3.30	2.97	2.89	2.76	3.25
Zr + Nb + Ce + Y	369	437	459	476	363	204	212	228	131	212	100	78.6	209	213	253	176
Y/Nb	0.42	0.43	0.44	0.42	0.43	0.29	0.33	0.26	0.19	0.44	0.18	0.16	0.41	0.45	0.36	0.36
Sr/Y	66.3	61.8	55.1	53.3	68.2	45.2	36.5	46.0	8.02	21.3	3.95	17.1	23.6	26.3	24.6	10.9
T _{Zr} (°C)	762	781	776	780	759	714	712	718	651	708	589	572	703	707	718	671

Notes: (1) Fe₂O₃^T is total Fe, and LOI is loss on ignition. (2) A/CNK is molar ratios Al₂O₃/(CaO + Na₂O + K₂O). (3) Mg[#] = 100Mg/(Mg + ΣFe) in mole. (4) Eu/Eu^{*} = 2Eu_N/(Sm_N + Gd_N), the chondrite values after Taylor and McLennan (1985). (5) T_{Zr} (°C) is zircon saturation temperature calculated using the geothermometer of Boehnke et al. (2013).

Technologies Analyte Excite laser-ablation system (Bozeman, Montana, USA) and Nu Instruments Nu Plasma II MC-ICP-MS (Wrexham, Wales, UK) were combined for the experiments. The 193 nm ArF excimer laser, homogenized by a set of beam delivery systems, was focused on zircon surface with fluence of 6.0J/cm². Ablation protocol employed a spot diameter of 50 µm at 8 Hz repetition rate for 40 s (equating to 320 pulses). Helium was applied as carrier gas to efficiently transport aerosol to MC-ICP-MS. The zircon standards Plešovice and Mud Tank were measured as quality control every eight analyses. They yielded average ¹⁷⁶Hf/¹⁷⁷Hf ratios of 0.282478 ± 8 (2σ, n = 9) and 0.282515 ± 11 (2σ, n = 9), respectively. These results are consistent with their recommended ¹⁷⁶Hf/¹⁷⁷Hf ratios within 2σ (0.282482 ± 13, Sláma et al., 2008; 0.282504 ± 44, Woodhead and Hergt, 2005).

4. Results

4.1. Major and trace elements

Major and trace element contents of the Wenjiaping and Wulaxi granites are presented in Table 1. The samples are characterized by relatively high SiO₂ (75.82–67.70 wt.%), Al₂O₃ (15.75–12.90 wt.%), Na₂O (5.21–3.62 wt.%) and K₂O (4.92–2.65 wt.%) contents. They have low Fe₂O₃^T (average 1.49 wt.%) and CaO (average 1.67 wt.%) concentrations. Other major oxides commonly occur lower than 1 wt.%. The major element contents are normalized to 100% on LOI-free basis before plotting them to diagrams. On the total alkali-silica (TAS), K₂O-SiO₂, and A/NK-A/CNK discriminant diagrams (Fig. 3b–d), the granite samples are high-K calc-alkaline and weakly peraluminous granite to

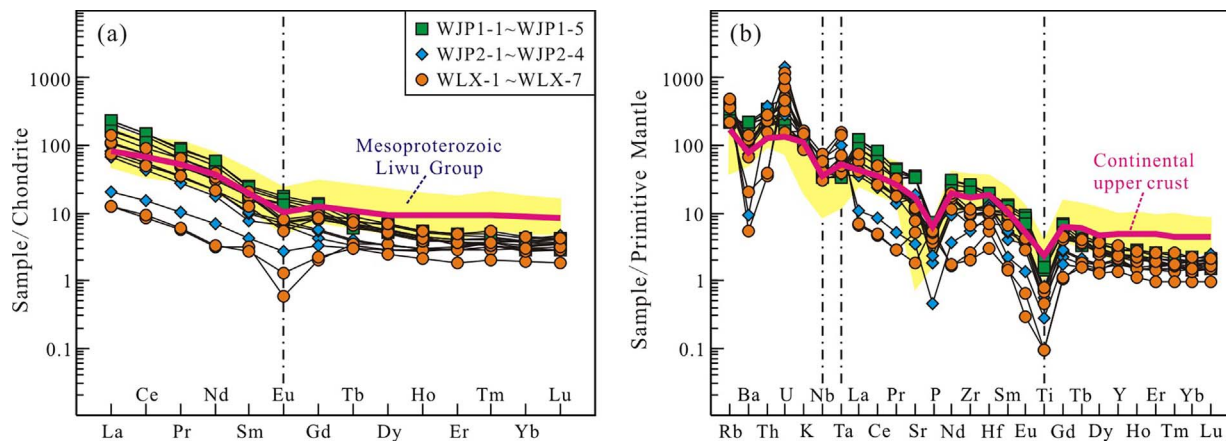


Fig. 4. REE (a) and trace element (b) diagrams, the values of chondrite, continental upper crust, primitive mantle and Liwu Group after Taylor and McLennan (1985), Sun and McDonough (1989) and Li et al. (2010), respectively.

granodiorite in composition.

The Wenjiaping and Wulaxi granites exhibit high La (average 41.8 ppm), Ce (average 71.5 ppm), Pr (average 6.48 ppm) and Nd (average 21.4 ppm) abundances, with different rare earth element contents (Σ REE = 297–20.3 ppm). Their chondrite-normalized REE profiles (Fig. 4a) are LREE-enriched ($(La/Yb)_N = 59.4\text{--}4.05$) with slightly negative Eu-anomalies (Eu/Eu* average 0.74). The samples have high concentrations of Rb (average 215 ppm), Sr (average 374 ppm), Ba (average 840 ppm) and Zr (average 144 ppm). Their primitive mantle-normalized trace element diagram (Fig. 4b) shows significant enrichment in large ion lithophile elements (LILEs, e.g., Rb, Sr and U) and depletion in high field strength elements (HFSEs, e.g., Nb, Ta and Ti). Their REE and trace element patterns resemble those of the continental upper crust (Taylor and McLennan, 1985) and the Mesoproterozoic Liwu Group (Li et al., 2010).

4.2. Zircon U-Pb geochronology

Zircon U-Pb dating data of the three granite samples (WJP1-1, WJP2-1 and WLX-1, Fig. 1b) are listed in Table 2. The zircons are mostly euhedral and up to 150 μm in length, with length to width ratios of ca. 2:1. Most of the zircons have high Th/U ratios (up to 3.71), and their CL images commonly show apparent oscillatory zoning (Fig. 5). These features are indicative of magmatic zircons (Hoskin and Schaltegger, 2003).

All the reported U-Pb isotopic data plot on or near the concordia curve. Twenty-two zircons from sample WJP1-1 yield $^{206}\text{Pb}/^{238}\text{U}$ ages of 176.9–161.3 Ma, with a weighted mean age of 164.5 ± 0.9 Ma ($n = 20$, MSWD = 2.9, Fig. 5a). Selected from sample WJP2-1, twenty-two zircons have $^{206}\text{Pb}/^{238}\text{U}$ ages of 167.2–154.2 Ma; their weighted mean age is 163.4 ± 0.9 Ma ($n = 18$, MSWD = 4.0, Fig. 5b). In addition, two inherited zircon grains (spots 11 and 12, Fig. 5c) from sample WLX-1 yield $^{207}\text{Pb}/^{206}\text{Pb}$ ages of 1450.9 Ma and 1203.4 Ma, respectively. Spots 17, 8 and 1 (inherited zircons, Fig. 5c) have $^{206}\text{Pb}/^{238}\text{U}$ ages of 622.8 Ma, 525.7 Ma and 260.3 Ma. Seventeen zircons yield $^{206}\text{Pb}/^{238}\text{U}$ ages between 172.7 Ma and 158.4 Ma, and a weighted mean age of 164.3 ± 1.7 Ma ($n = 13$, MSWD = 6.0, Fig. 5d).

4.3. Zircon Hf isotopic compositions

Zircon Hf isotopic data are presented in Table 3. The $\epsilon_{\text{Hf}}(t)$ values were calculated using their respective $^{206}\text{Pb}/^{238}\text{U}$ ages, except for spots WLX-1.11 and WLX-1.12 using their $^{207}\text{Pb}/^{206}\text{Pb}$ ages. Two inherited 1450.9–1203.4 Ma zircons yield $\epsilon_{\text{Hf}}(t)$ values of 1.7 and –2.0, and two-stage Hf model ages (T_{DM2}) of 2120–2088 Ma. Two 622.8–525.7 Ma zircons have $\epsilon_{\text{Hf}}(t)$ values of 1.6 and 3.3, and T_{DM2} of 1462 Ma and 1280

Ma, respectively. The 260.3 Ma zircon show $\epsilon_{\text{Hf}}(t)$ value of –2.0 and T_{DM2} of 1416 Ma. Sixty-one 176.9–154.2 Ma zircons yield T_{DM2} of 2102–1122 Ma; their $\epsilon_{\text{Hf}}(t)$ values vary from 1.4 to –13.9, mostly below the chondrite uniform reservoir curve (Fig. 6).

5. Discussion

5.1. Emplacement ages

Previous studies proposed that the Rodinia supercontinent assembled through worldwide orogenic events at ca. 1300–900 Ma, and its breakup occurred at ca. 860–570 Ma which may have led to the birth of the Gondwana supercontinent at ca. 600–530 Ma (Li et al., 2008). The SGO was considered to have been built on oceanic crust above a west-dipping subduction zone, and later collided with the western Yangtze Block (Zhou et al., 2002). Zircon U-Pb geochronological data uncovered that the Proterozoic evolution of these tectonic units was closely associated with the abovementioned two supercontinents (Zhou et al., 2002; Roger et al., 2010; Chen et al., 2016). In this paper, four inherited zircons from sample WLX-1 yield U-Pb ages of 1450.9 Ma, 1203.4 Ma, 622.8 Ma and 525.7 Ma, respectively (Fig. 5c), with $\epsilon_{\text{Hf}}(t)$ values between 3.3 and –2.0 (Fig. 6). These ages can be correlated with the Rodinia and Gondwana supercontinents globally. In addition, one inherited zircon has $^{206}\text{Pb}/^{238}\text{U}$ age of 260.3 Ma and $\epsilon_{\text{Hf}}(t)$ value of –2.0. This age was most likely associated with the ca. 260 Ma Emeishan large igneous province in the western margin of the Yangtze Block (Xiao et al., 2004). Significantly, other magmatic zircons yield weighted mean ages of 164.5 ± 0.9 Ma and 163.4 ± 0.9 Ma for samples WJP1-1 and WJP2-1, and 164.3 ± 1.7 Ma for sample WLX-1 (Fig. 5). These are the best estimates for the emplacement ages of the Wenjiaping and Wulaxi granite plutons, and indicate that they were formed during the same magmatic event.

5.2. Alteration effects on whole-rock compositions

The effect of alteration and mobility of major and trace elements must be evaluated before we discuss the granite petrogenesis. Warren et al. (2007) introduced the K/Al vs. $(2\text{Ca} + \text{Na} + \text{K})/\text{Al}$ diagram to evaluate the alteration effects. On this diagram, all the samples have high $(2\text{Ca} + \text{Na} + \text{K})/\text{Al}$ ratios (Fig. 7a), which indicates that they are the least altered rocks (Dai et al., 2014). Zirconium is generally considered to be the most immobile element during low-grade alteration of igneous rocks, and can be used to evaluate the alteration effects on their chemical composition (Polat et al., 2002). In this study, the granite samples commonly display fairly good correlations between Zr and major elements (e.g., TiO_2 , Fe_2O_3^T , MgO and CaO), REEs and HFSEs (Fig. 7b–g). Therefore, we advocate that the granite chemical

Table 2

Zircon U-Pb isotopic data of the granite samples WJP1-1, WJP2-1 and WLX-1.

Spots	Th (ppm)	U (ppm)	Th/U	$^{207}\text{Pb}/^{206}\text{Pb}$	$\pm \sigma$	$^{207}\text{Pb}/^{235}\text{U}$	$\pm \sigma$	$^{206}\text{Pb}/^{238}\text{U}$	$\pm \sigma$	$^{207}\text{Pb}/^{206}\text{Pb}$	$\pm \sigma$	$^{207}\text{Pb}/^{235}\text{U}$	$\pm \sigma$	$^{206}\text{Pb}/^{238}\text{U}$	$\pm \sigma$
Sample WJP1-1, the Wenjiaping granite															
WJP1-1.1	2480	3471	0.71	0.0520	0.0008	0.1849	0.0027	0.0257	0.0001	283.4	33.3	172.3	2.3	163.9	0.9
WJP1-1.2	776	1111	0.70	0.0495	0.0013	0.1898	0.0052	0.0278	0.0002	168.6	63.0	176.5	4.4	176.9	1.5
WJP1-1.3	245	993	0.25	0.0496	0.0011	0.1762	0.0038	0.0258	0.0002	176.0	56.5	164.8	3.3	164.3	1.0
WJP1-1.4	163	857	0.19	0.0527	0.0012	0.1889	0.0042	0.0261	0.0002	322.3	51.8	175.7	3.6	166.2	1.2
WJP1-1.5	323	2101	0.15	0.0500	0.0008	0.1771	0.0030	0.0257	0.0002	198.2	34.3	165.6	2.6	163.3	1.0
WJP1-1.6	289	1256	0.23	0.0500	0.0013	0.1740	0.0043	0.0254	0.0002	194.5	59.2	162.9	3.7	162.0	1.4
WJP1-1.7	143	828	0.17	0.0474	0.0015	0.1713	0.0051	0.0265	0.0002	77.9	64.8	160.5	4.4	168.8	1.5
WJP1-1.8	343	1160	0.30	0.0492	0.0011	0.1736	0.0037	0.0255	0.0002	166.8	50.0	162.5	3.2	162.5	1.0
WJP1-1.9	408	1145	0.36	0.0493	0.0013	0.1777	0.0046	0.0263	0.0002	161.2	61.1	166.1	4.0	167.3	1.3
WJP1-1.10	209	923	0.23	0.0502	0.0018	0.1759	0.0058	0.0259	0.0002	211.2	83.3	164.5	5.0	164.5	1.5
WJP1-1.11	842	3322	0.25	0.0490	0.0007	0.1746	0.0024	0.0258	0.0001	146.4	33.3	163.4	2.1	164.1	0.9
WJP1-1.12	400	1375	0.29	0.0494	0.0009	0.1723	0.0032	0.0253	0.0001	164.9	44.4	161.4	2.8	161.3	0.9
WJP1-1.13	386	954	0.40	0.0494	0.0012	0.1778	0.0041	0.0261	0.0002	168.6	55.5	166.1	3.5	166.2	1.1
WJP1-1.14	294	1284	0.23	0.0494	0.0011	0.1768	0.0039	0.0261	0.0002	168.6	49.1	165.3	3.3	165.8	1.1
WJP1-1.15	1043	1820	0.57	0.0494	0.0011	0.1801	0.0042	0.0265	0.0002	164.9	47.2	168.2	3.6	168.4	1.3
WJP1-1.16	534	2328	0.23	0.0482	0.0008	0.1714	0.0027	0.0258	0.0002	109.4	37.0	160.6	2.3	164.2	1.0
WJP1-1.17	203	798	0.25	0.0497	0.0015	0.1809	0.0053	0.0266	0.0002	189.0	70.4	168.8	4.6	169.0	1.2
WJP1-1.18	178	1022	0.17	0.0494	0.0011	0.1759	0.0040	0.0259	0.0002	164.9	53.7	164.5	3.5	164.7	1.3
WJP1-1.19	91	620	0.15	0.0500	0.0013	0.1774	0.0047	0.0258	0.0002	194.5	63.0	165.8	4.1	164.4	1.5
WJP1-1.20	6848	4583	1.49	0.0496	0.0007	0.1762	0.0025	0.0257	0.0002	176.0	33.3	164.8	2.2	163.9	1.3
WJP1-1.21	298	957	0.31	0.0518	0.0012	0.1838	0.0044	0.0258	0.0002	276.0	53.7	171.4	3.8	164.0	1.5
WJP1-1.22	517	1762	0.29	0.0530	0.0010	0.1882	0.0036	0.0257	0.0002	327.8	42.6	175.1	3.0	163.7	1.4
Sample WJP2-1, the Wenjiaping granite															
WJP2-1.1	10218	4699	2.17	0.0491	0.0006	0.1763	0.0021	0.0260	0.0001	153.8	30.6	164.9	1.8	165.3	0.9
WJP2-1.2	748	1958	0.38	0.0493	0.0008	0.1759	0.0027	0.0259	0.0001	166.8	35.2	164.5	2.4	164.7	0.9
WJP2-1.3	715	2694	0.27	0.0514	0.0009	0.1856	0.0026	0.0263	0.0001	257.5	40.7	172.9	2.2	167.2	0.9
WJP2-1.4	11803	12478	0.95	0.0484	0.0005	0.1722	0.0017	0.0258	0.0001	116.8	22.2	161.3	1.5	164.0	0.9
WJP2-1.5	27508	7414	3.71	0.0501	0.0005	0.1773	0.0019	0.0256	0.0001	198.2	28.7	165.7	1.7	163.0	0.8
WJP2-1.6	200	1210	0.17	0.0547	0.0010	0.1975	0.0037	0.0262	0.0002	398.2	36.1	183.0	3.1	166.6	1.0
WJP2-1.7	827	3937	0.21	0.0468	0.0007	0.1625	0.0023	0.0252	0.0001	39.0	−163.9	152.9	2.0	160.2	0.8
WJP2-1.8	826	1702	0.49	0.0472	0.0010	0.1660	0.0035	0.0256	0.0002	61.2	50.0	156.0	3.0	163.1	1.3
WJP2-1.9	3921	3942	0.99	0.0490	0.0008	0.1719	0.0030	0.0254	0.0002	150.1	32.4	161.1	2.6	161.6	1.3
WJP2-1.10	452	2009	0.22	0.0472	0.0008	0.1636	0.0027	0.0251	0.0001	61.2	40.7	153.9	2.3	160.0	0.8
WJP2-1.11	900	3643	0.25	0.0505	0.0007	0.1798	0.0027	0.0257	0.0001	220.4	33.3	167.9	2.3	163.7	0.9
WJP2-1.12	913	2995	0.30	0.0500	0.0007	0.1762	0.0023	0.0255	0.0001	198.2	31.5	164.8	2.0	162.3	0.8
WJP2-1.13	539	1897	0.28	0.0522	0.0013	0.1791	0.0044	0.0253	0.0002	294.5	53.7	167.2	3.8	160.8	1.2
WJP2-1.14	2029	3490	0.58	0.0480	0.0006	0.1662	0.0021	0.0251	0.0001	101.9	25.0	156.1	1.8	159.6	0.7
WJP2-1.15	165	1190	0.14	0.0478	0.0012	0.1715	0.0042	0.0262	0.0002	87.1	56.5	160.7	3.6	166.7	1.3
WJP2-1.16	2076	7915	0.26	0.0546	0.0011	0.1909	0.0046	0.0255	0.0002	398.2	42.6	177.4	3.9	162.6	1.4
WJP2-1.17	8991	4462	2.02	0.0493	0.0007	0.1643	0.0022	0.0242	0.0001	166.8	33.3	154.5	1.9	154.2	0.9
WJP2-1.18	341	1905	0.18	0.0486	0.0008	0.1743	0.0028	0.0260	0.0001	127.9	38.9	163.2	2.5	165.3	0.8
WJP2-1.19	1483	3760	0.39	0.0488	0.0006	0.1743	0.0021	0.0259	0.0001	200.1	27.8	163.1	1.8	164.5	0.8
WJP2-1.20	1072	2692	0.40	0.0460	0.0009	0.1619	0.0032	0.0257	0.0002	483.4	254.6	152.3	2.8	163.6	1.4
WJP2-1.21	2183	4803	0.45	0.0484	0.0006	0.1725	0.0022	0.0259	0.0001	116.8	31.5	161.6	1.9	164.6	0.9
WJP2-1.22	2846	2700	1.05	0.0525	0.0009	0.1884	0.0036	0.0258	0.0002	305.6	40.7	175.2	3.1	164.4	1.0
Sample WLX-1, the Wulaxi granite															
WLX-1.1	676	741	0.91	0.0553	0.0012	0.3122	0.0066	0.0412	0.0003	433.4	50.0	275.9	5.1	260.3	1.9
WLX-1.2	119	2907	0.04	0.0494	0.0008	0.1775	0.0029	0.0261	0.0001	168.6	38.9	165.9	2.5	165.8	0.9
WLX-1.3	271	2722	0.10	0.0523	0.0009	0.1928	0.0030	0.0267	0.0002	298.2	41.7	179.1	2.6	169.7	0.9
WLX-1.4	158	1004	0.16	0.0497	0.0013	0.1760	0.0045	0.0258	0.0002	189.0	61.1	164.6	3.8	164.5	1.1
WLX-1.5	753	2564	0.29	0.0498	0.0010	0.1749	0.0034	0.0255	0.0002	187.1	48.1	163.7	2.9	162.6	1.1
WLX-1.6	497	4099	0.12	0.0489	0.0006	0.1705	0.0020	0.0252	0.0001	142.7	23.1	159.8	1.7	160.4	0.8
WLX-1.7	169	1238	0.14	0.0496	0.0010	0.1802	0.0036	0.0264	0.0002	189.0	52.8	168.2	3.1	168.3	1.2
WLX-1.8	153	456	0.34	0.0578	0.0016	0.6741	0.0271	0.0850	0.0002	524.1	59.3	523.2	16.4	525.7	15.8
WLX-1.9	177	1601	0.11	0.0494	0.0012	0.1820	0.0044	0.0267	0.0002	168.6	62.0	169.8	3.8	169.8	1.5
WLX-1.10	321	3184	0.10	0.0495	0.0007	0.1855	0.0027	0.0271	0.0002	172.3	2.8	172.8	2.3	172.7	1.1
WLX-1.11	160	448	0.36	0.0912	0.0013	3.1703	0.0456	0.2523	0.0018	1450.9	23.1	1450.0	11.1	1450.4	9.3
WLX-1.12	767	874	0.88	0.0803	0.0013	2.2460	0.0563	0.2032	0.0041	1203.4	31.5	1195.5	17.6	1192.3	22.0
WLX-1.13	217	827	0.26	0.0506	0.0017	0.1781	0.0059	0.0258	0.0002	220.4	79.6	166.4	5.1	164.4	1.3
WLX-1.14	78	637	0.12	0.0498	0.0013	0.1744	0.0045	0.0257	0.0002	183.4	67.6	163.2	3.9	163.4	1.4
WLX-1.15	1167	6905	0.17	0.0497	0.0008	0.1840	0.0028	0.0270	0.0002	189.0	37.0	171.5	2.4	171.7	1.2
WLX-1.16	112	378	0.30	0.0506	0.0014	0.1726	0.0050	0.0249	0.0002	220.4	58.3	161.6	4.3	158.4	1.3
WLX-1.17	122	293	0.42	0.0612	0.0013	0.8535	0.0178	0.1014	0.0007	655.6	50.9	626.6	9.7	622.8	4.2
WLX-1.18	322	1601	0.20	0.0											

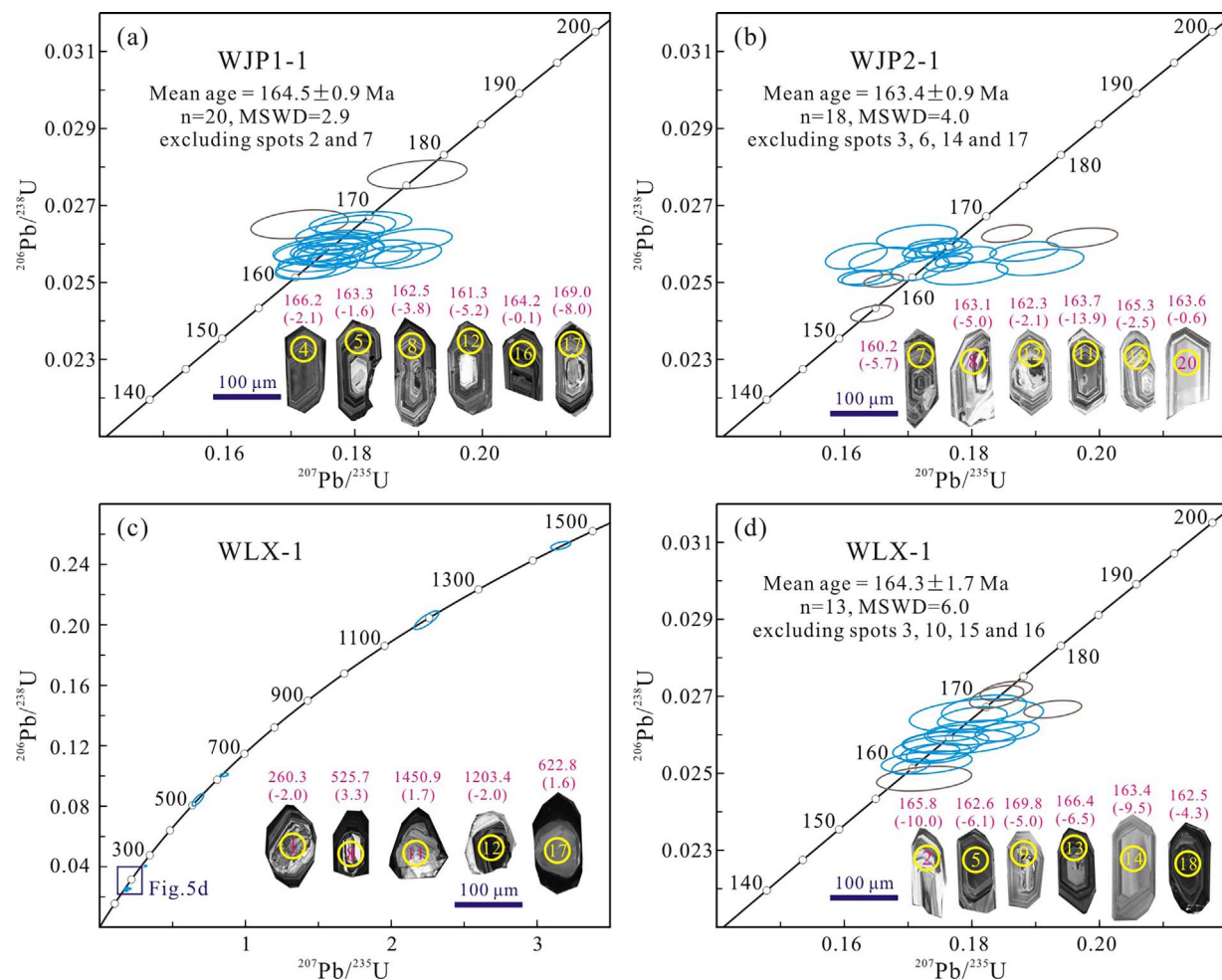


Fig. 5. Concordia plots of zircon U-Pb data and representative CL images with U-Pb ages and $\epsilon_{\text{Hf}}(t)$ values.

compositions were insignificantly influenced by subsequent alteration, and our geochemical data can be used to explore the granite petrogenesis.

5.3. Genetic type: an I-type affinity

The Wenjiaping and Wulaxi granites lack typical peraluminous minerals, e.g. primary garnet, cordierite, muscovite, sillimanite and andalusite, and ilmenite instead of magnetite (Fig. 2). They have low A/CNK ratios of 1.10–0.99 (Fig. 3d) and high Na₂O contents of 5.21–3.62 wt.% in composition. These petrological and geochemical features rule out an affinity with S-type granites, which commonly contain Al-rich minerals with high A/CNK values (> 1.1) and low Na₂O contents (Chappell, 1999).

The granite samples show high Ga/Al ratios ($10000 \times \text{Ga}/\text{Al} = 3.68\text{--}2.58$, Table 1) and thus resemble those of A-type granites. However, they have relatively low FeO^T/MgO ratios (8.55–2.83) and Zr + Nb + Ce + Y concentrations (average 258 ppm). Their geochemical characteristics are different from those of typical A-type granites ($\text{FeO}^T/\text{MgO} > 11$, Zr + Nb + Ce + Y > 350 ppm, Whalen et al., 1987). Zircon saturation thermometry provides a robust way to estimate magma temperatures from whole-rock compositions (Watson and Harrison, 1983; Boehnke et al., 2013). In this paper, zircon saturation temperatures were calculated using the new thermometer proposed by Boehnke et al. (2013). Because two samples WLX-2 and WLX-3 are strongly depleted in Zr contents (29.0 ppm and 23.0 ppm), their magma temperatures are extremely low (589 °C and 572 °C). The other granite samples show zircon saturation temperatures in the range

of 781–651 °C with an average of 726 °C (Table 1). These data are entirely against the high-temperature formation conditions of A-type granites (> 800 °C, King et al., 1997). In addition, A-type granites typically contain pyroxene and fayalite, and late-crystallizing (interstitial) biotite and amphibole (King et al., 1997). However, these mineral assemblages have not been identified by our petrographical observations (Fig. 2).

The granite samples are metaluminous to weakly peraluminous (Fig. 3d), and show negative trends on the Al₂O₃ and P₂O₅ vs. SiO₂ plot (Fig. 9e and g). These features agree with those of I-type granites (Chappell, 1999). I-type granites always contain hornblende, especially at the more mafic end of the compositional spectrum (Chappell et al., 2012), and hornblende is present in petrographic thin sections (Fig. 2i). Thus, their chemical compositions and mineral assemblages indicate an I-type affinity (Fig. 8a). Chappell and White (1974) defined the I-type granite as a result of partial melting of igneous source rocks. On the K₂O/Na₂O vs. CaO/(MgO + FeO^T) diagram, all the samples plot in the field of metabasalts and metaandesites (Fig. 8b), and thus fit the I-type definition. Therefore, we classify the Wenjiaping and Wulaxi granites as I-type, rather than S- or A-type.

5.4. Petrogenesis of the granites

Many compositional variations have been identified for I-type granites, and there is no consensus on their origin. Prior studies uncovered that I-type granites were mainly attributed to three petrogenetic scenarios, including (1) a complete process of fractional crystallization from primary mafic magmas (Cawthorn and Brown, 1976;

Table 3

Zircon Lu-Hf isotopes of the three dated granite samples.

Spots	Age (Ma)	$^{176}\text{Yb}/^{177}\text{Hf}$	$^{176}\text{Lu}/^{177}\text{Hf}$	$^{176}\text{Hf}/^{177}\text{Hf}$	$\pm 2\sigma$	$\varepsilon_{\text{Hf}}(\text{t})$	T_{DM1} (Ma)	T_{DM2} (Ma)
Sample WJP1-1, the Wenjiaping granite								
WJP1-1.1	163.9	0.069977	0.002181	0.282311	0.000020	-13.0	1375	2038
WJP1-1.2	176.9	0.024252	0.000566	0.282671	0.000017	0.2	817	1211
WJP1-1.3	164.3	0.031005	0.001017	0.282582	0.000012	-3.3	952	1423
WJP1-1.4	166.2	0.030213	0.000951	0.282613	0.000014	-2.1	907	1351
WJP1-1.5	163.3	0.026248	0.000770	0.282630	0.000016	-1.6	879	1315
WJP1-1.6	162.0	0.029280	0.000781	0.282657	0.000015	-0.7	842	1255
WJP1-1.7	168.8	0.012734	0.000395	0.282592	0.000010	-2.8	924	1395
WJP1-1.8	162.5	0.019514	0.000672	0.282568	0.000010	-3.8	964	1454
WJP1-1.9	167.3	0.032566	0.000800	0.282620	0.000013	-1.9	894	1335
WJP1-1.10	164.5	0.053994	0.001268	0.282611	0.000011	-2.3	917	1359
WJP1-1.11	164.1	0.037519	0.001379	0.282598	0.000011	-2.8	939	1390
WJP1-1.12	161.3	0.033165	0.000960	0.282529	0.000010	-5.2	1025	1544
WJP1-1.13	166.2	0.024346	0.000619	0.282641	0.000011	-1.1	860	1287
WJP1-1.14	165.8	0.018320	0.000575	0.282682	0.000011	0.3	802	1194
WJP1-1.15	168.4	0.086054	0.002437	0.282375	0.000016	-10.7	1292	1895
WJP1-1.16	164.2	0.024647	0.000700	0.282673	0.000011	-0.1	818	1217
WJP1-1.17	169.0	0.020896	0.000680	0.282446	0.000012	-8.0	1134	1724
WJP1-1.18	164.7	0.029550	0.000883	0.282590	0.000013	-3.0	938	1404
WJP1-1.19	164.4	0.031344	0.000720	0.282715	0.000011	1.4	759	1122
WJP1-1.20	163.9	0.091323	0.002024	0.282388	0.000016	-10.3	1259	1867
WJP1-1.21	164.0	0.016568	0.000515	0.282700	0.000010	0.9	775	1154
WJP1-1.22	163.7	0.030584	0.000936	0.282545	0.000010	-4.6	1002	1506
Sample WJP2-1, the Wenjiaping granite								
WJP2-1.1	165.3	0.042209	0.001336	0.282485	0.000011	-6.8	1099	1644
WJP2-1.2	164.7	0.037106	0.001192	0.282488	0.000016	-6.6	1090	1636
WJP2-1.3	167.2	0.023875	0.000839	0.282634	0.000013	-1.4	874	1302
WJP2-1.4	164.0	0.041827	0.001437	0.282529	0.000012	-5.2	1038	1545
WJP2-1.5	163.0	0.058094	0.001719	0.282403	0.000014	-9.7	1228	1832
WJP2-1.6	166.6	0.020490	0.000760	0.282587	0.000013	-3.0	939	1408
WJP2-1.7	160.2	0.043611	0.001488	0.282517	0.000012	-5.7	1057	1575
WJP2-1.8	163.1	0.034283	0.001045	0.282535	0.000011	-5.0	1019	1529
WJP2-1.9	161.6	0.099088	0.003367	0.282312	0.000017	-13.1	1419	2045
WJP2-1.10	160.0	0.028714	0.000957	0.282659	0.000013	-0.7	843	1253
WJP2-1.11	163.7	0.088122	0.002238	0.282285	0.000013	-13.9	1415	2097
WJP2-1.12	162.3	0.029687	0.001033	0.282617	0.000013	-2.1	904	1347
WJP2-1.13	160.8	0.022775	0.000802	0.282631	0.000012	-1.6	878	1314
WJP2-1.14	159.6	0.061245	0.001874	0.282390	0.000017	-10.3	1250	1862
WJP2-1.15	166.7	0.021144	0.000668	0.282638	0.000012	-1.2	866	1294
WJP2-1.16	162.6	0.045167	0.001416	0.282449	0.000013	-8.1	1151	1725
WJP2-1.17	154.2	0.031843	0.001224	0.282510	0.000012	-6.1	1059	1592
WJP2-1.18	165.3	0.025088	0.000928	0.282602	0.000011	-2.5	921	1376
WJP2-1.19	164.5	0.061080	0.001754	0.282505	0.000014	-6.1	1083	1602
WJP2-1.20	163.6	0.022451	0.000744	0.282659	0.000012	-0.6	838	1249
WJP2-1.21	164.6	0.042086	0.001480	0.282544	0.000014	-4.7	1019	1512
WJP2-1.22	164.4	0.028050	0.000798	0.282644	0.000015	-1.1	860	1282
Sample WLX-1, the Wulaxi granite								
WLX-1.1	260.3	0.054327	0.001439	0.282562	0.000014	-2.0	992	1416
WLX-1.2	165.8	0.048478	0.001464	0.282394	0.000013	-10.0	1231	1847
WLX-1.3	169.7	0.040637	0.001452	0.282404	0.000015	-9.5	1217	1823
WLX-1.4	164.5	0.015733	0.000550	0.282483	0.000011	-6.7	1078	1643
WLX-1.5	162.6	0.044559	0.001478	0.282504	0.000013	-6.1	1075	1603
WLX-1.6	160.4	0.049238	0.001340	0.282520	0.000013	-5.6	1048	1567
WLX-1.7	168.3	0.039284	0.001188	0.282569	0.000011	-3.7	976	1452
WLX-1.8	525.7	0.024803	0.000819	0.282548	0.000013	3.3	995	1280
WLX-1.9	169.8	0.039625	0.001239	0.282530	0.000014	-5.0	1032	1538
WLX-1.10	172.7	0.036663	0.001183	0.282278	0.000013	-13.9	1386	2102
WLX-1.11	1450.9	0.044783	0.001352	0.281949	0.000011	1.7	1853	2088
WLX-1.12	1203.4	0.032895	0.000958	0.281994	0.000014	-2.0	1772	2120
WLX-1.13	164.4	0.026886	0.000705	0.282490	0.000016	-6.5	1073	1627
WLX-1.14	163.4	0.011636	0.000341	0.282405	0.000013	-9.5	1180	1817
WLX-1.15	171.7	0.034277	0.001127	0.282488	0.000011	-6.5	1087	1630
WLX-1.16	158.4	0.017310	0.000522	0.282560	0.000012	-4.1	970	1473
WLX-1.17	622.8	0.022145	0.000662	0.282439	0.000013	1.6	1143	1462
WLX-1.18	162.5	0.046860	0.001407	0.282556	0.000013	-4.3	999	1485
WLX-1.19	161.1	0.012615	0.000341	0.282541	0.000017	-4.7	992	1513
WLX-1.20	166.1	0.052690	0.001502	0.282582	0.000012	-3.3	965	1426
WLX-1.21	165.9	0.042666	0.001278	0.282547	0.000012	-4.5	1009	1504
WLX-1.22	168.7	0.034353	0.001055	0.282526	0.000010	-5.2	1032	1546

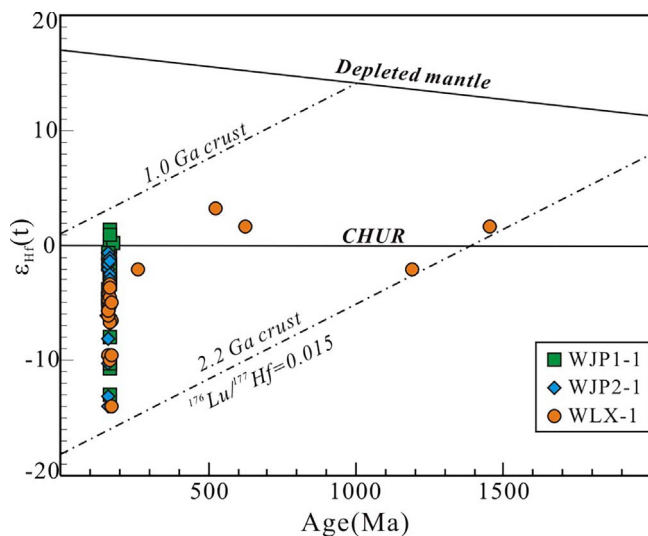


Fig. 6. Plot of $\epsilon_{\text{Hf}}(t)$ vs. individual crystallization age of analyzed zircons. CHUR = chondrite uniform reservoir.

(Wyborn et al., 1987); (2) partial melting of crustal materials and subsequent fractional crystallization (Turpin et al., 1990; Barbarin, 1996; Chappell et al., 2012); and (3) mixing of mantle-derived and crustal melts (Castro et al., 1991).

In the present study, the Wenjiaping and Wulaxi granites have LILEs enrichment and HFSEs depletion, and they show REE patterns and trace element profiles resembling those of the continental upper crust (Fig. 4). These geochemical features are indicative of derivation from crustal melts (Barth et al., 2000). $Mg^{\#}$ value is a useful index for discriminating melts of purely crustal origin ($Mg^{\#} < 40$) from those interacted with mantle-derived magmas ($Mg^{\#} > 40$, Rapp and Watson, 1995). In this paper, all the samples have relatively low $Mg^{\#}$ values of 38.7–17.3 (Table 1), implying the absence of mantle-derived components. However, the granites have Y/Nb ratios lower than 1.2 (Table 1), implying that they have a deeper origin (Eby, 1992). Based on zircon U-Pb chronology, several inherited zircons were detected within the Wulaxi granite (Fig. 5c), and they are commonly interpreted to be a key symbol of ancient crust remelting (Tchameni et al., 2001). Hf isotopic analyses yield T_{DM2} of 2102–1122 Ma with mostly negative $\epsilon_{\text{Hf}}(t)$ values from 1.4 to –13.9 for the 176.9–154.2 Ma zircons within the Wenjiaping and Wulaxi granites (Table 3). All zircons plot between the 2.2 Ga and 1.0 Ga crustal evolution lines (Fig. 6), indicating a main derivation from reworking of the Proterozoic crust, such as the Mesoproterozoic Liwu Group with similar REE and trace element patterns (Fig. 4). However, several zircons (e.g., WJP1-1.19) have positive $\epsilon_{\text{Hf}}(t)$ values above the chondrite uniform reservoir curve, suggesting minor involvement of a juvenile crust. This is also consistent with low Y/Nb ratios (0.45–0.16) of the granite samples. Therefore, we suggest that two granites were derived from remelting of ancient crust ($\epsilon_{\text{Hf}}(t) < 0$) with minor addition of juvenile crust ($\epsilon_{\text{Hf}}(t) > 0$). This viewpoint is

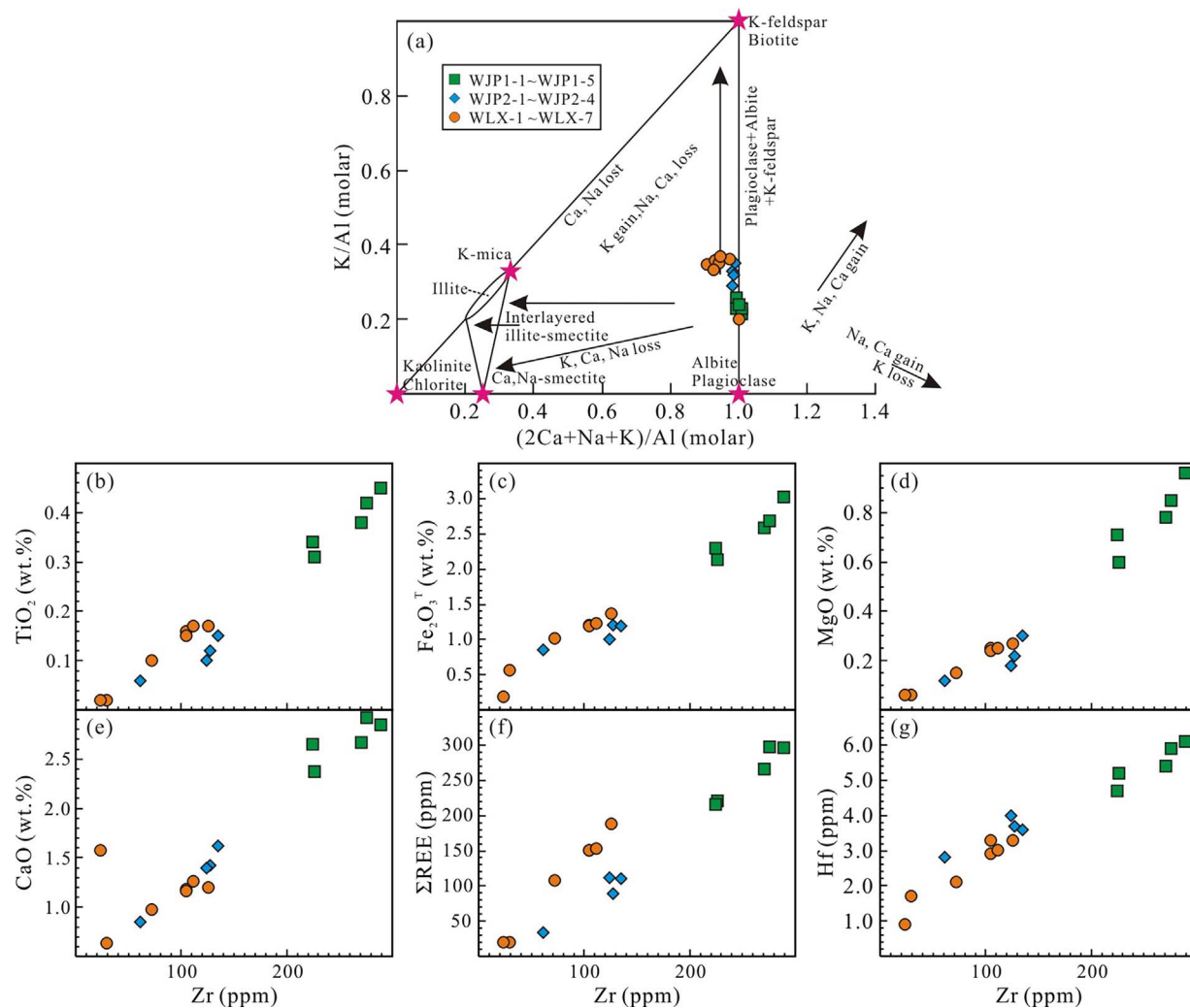


Fig. 7. (a) Molar element ratio plot of K/Al vs. $(2\text{Ca} + \text{Na} + \text{K})/\text{Al}$ (Warren et al., 2007). (b-g) Zr and selected major and trace element Harker variation diagrams.

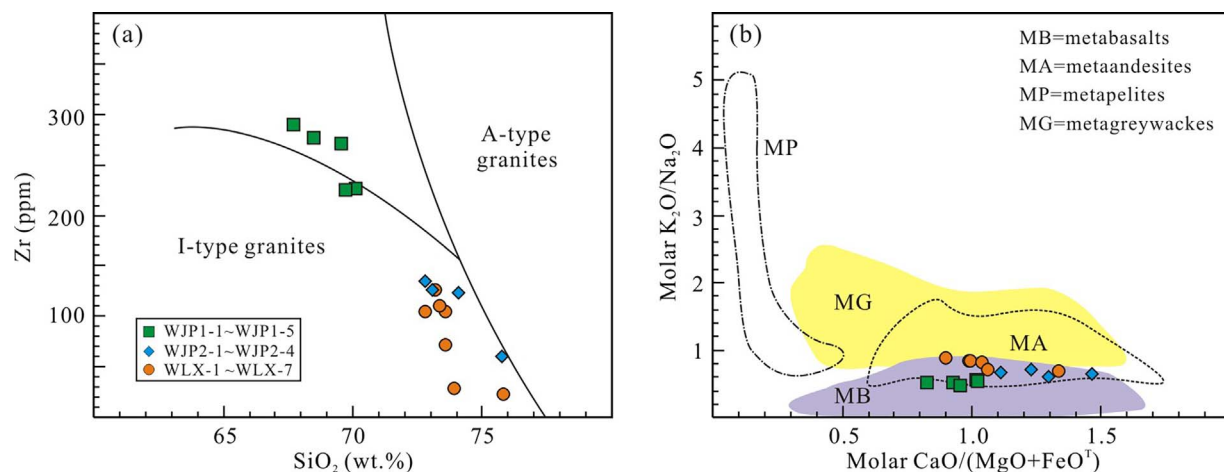


Fig. 8. (a) Zr vs. SiO_2 diagram (Collins et al., 1982). (b) Molar $\text{K}_2\text{O}/\text{Na}_2\text{O}$ vs. molar $\text{CaO}/(\text{MgO} + \text{FeO}^{\text{T}})$ diagram (Altherr and Siebel, 2002).

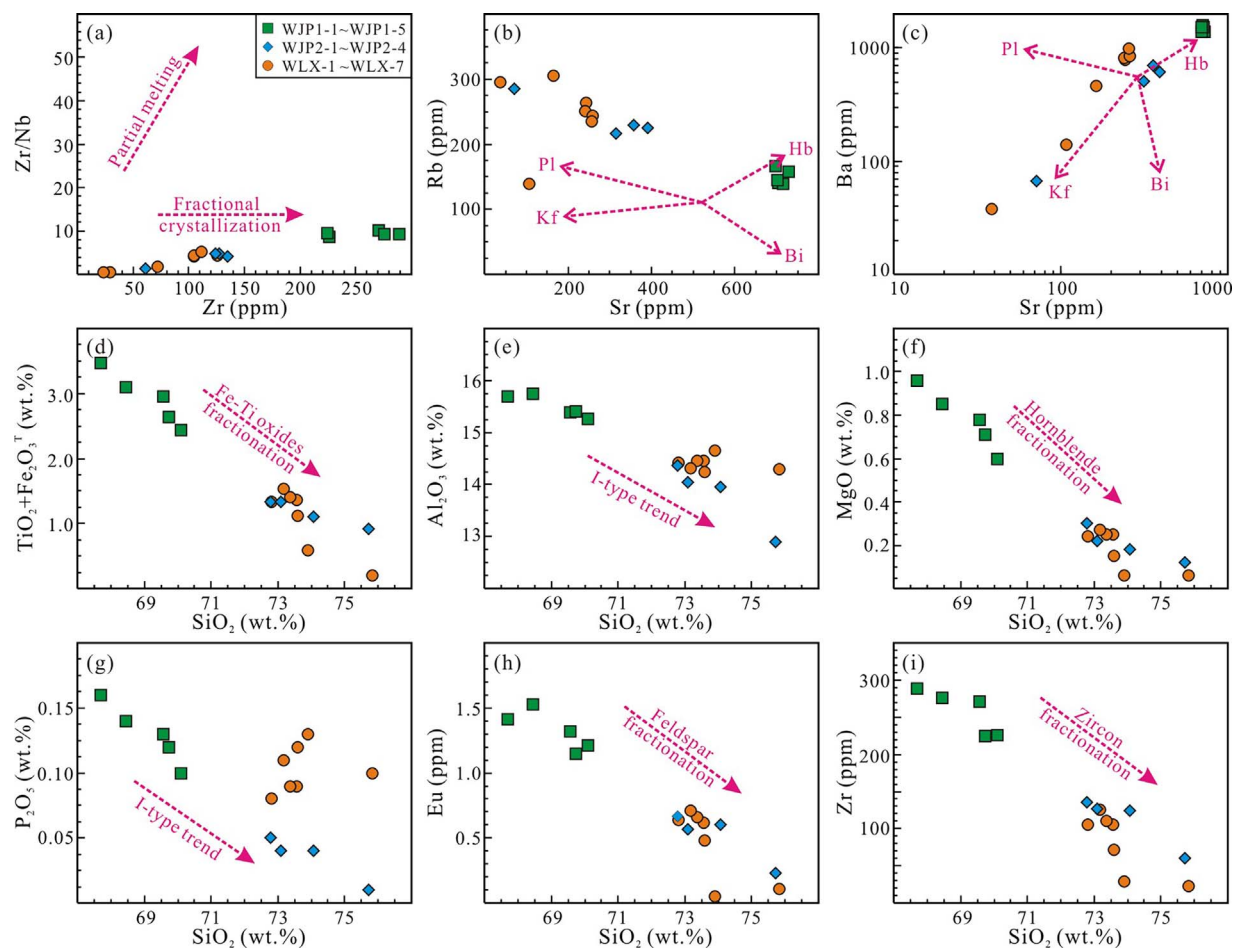


Fig. 9. (a) Zr/Nb vs. Zr diagram for the granite evolution (Geng et al., 2009). (b-i) Major and trace element Harker variation diagrams showing the magmatic evolution. Pl = plagioclase; Kf = K-feldspar; Hb = hornblende; Bi = biotite.

further supported by the absence of coeval mafic rocks in this region (SBGMR, 1991; Yan et al., 1997).

Prior studies have indicated that silicic magmas are dominantly produced by fractional crystallization (Dall'Agnol et al., 1999), which is illuminated by the Zr/Nb vs. Zr diagram of our granite samples (Fig. 9a). The granites have a wide range of SiO_2 contents (75.82–67.70 wt.%), and some major oxides and trace elements show systematic variations on the Harker diagrams (Fig. 9). These

geochemical signatures indicate that fractional crystallization might play a predominant role during magmatic evolution. According to covariations between Rb, Ba and Sr (Figs. 9b–c), together with decreases in Al_2O_3 , MgO and Eu with increasing SiO_2 (Fig. 9e, f and h), a fractional assemblage of feldspar and hornblende was evident. However, the samples exhibit slightly negative Eu-anomalies (Eu/Eu^* average 0.74) and HREE depletion ($(\text{La}/\text{Yb})_N = 59.4\text{--}4.05$, Fig. 4a), indicating the presence of garnet rather than feldspar as a main residual

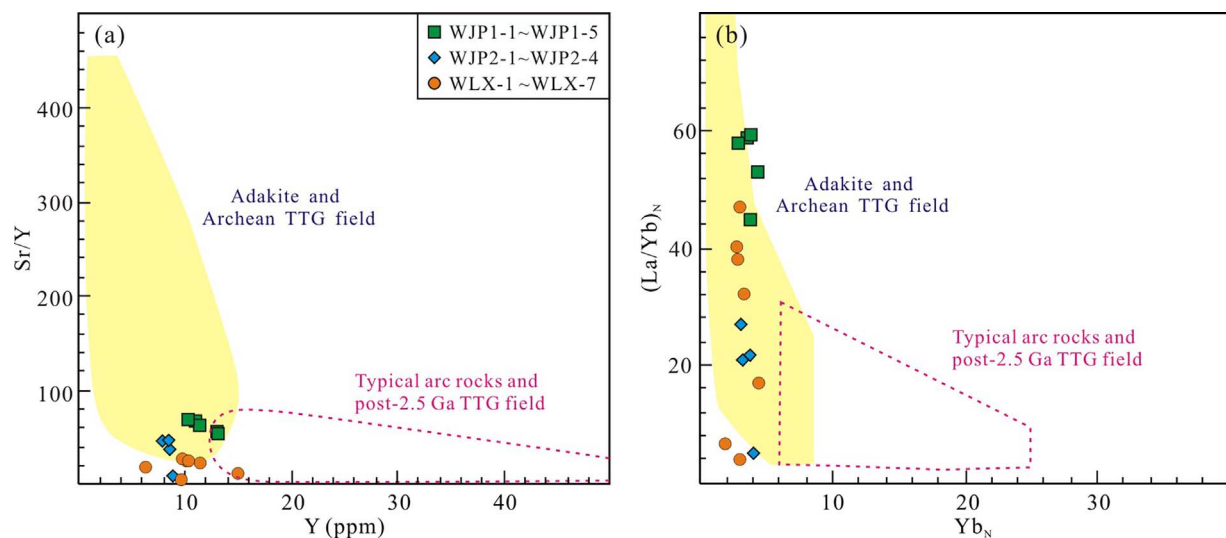


Fig. 10. (a) Sr/Y vs. Y (Defant and Drummond, 1990) diagram. (b) (La/Yb)_N vs. Yb_N (Martin, 1986) diagram, the chondrite values after Taylor and McLennan (1985).

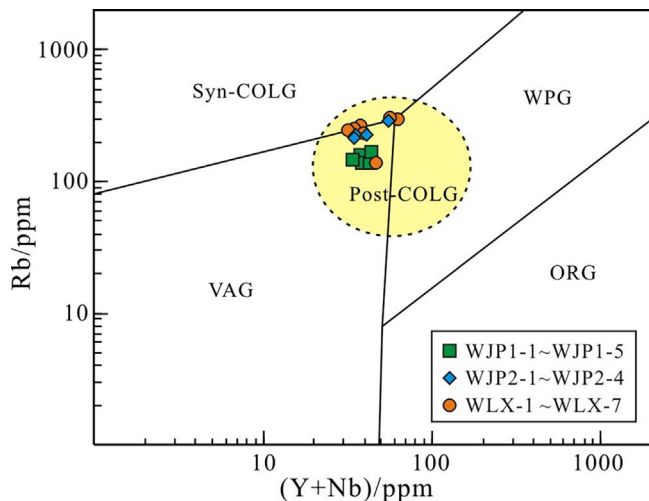


Fig. 11. Tectonic discrimination diagrams for the Wenjiaping and Wulaxi granites, after Pearce et al. (1984).

mineral in the magma source (Defant and Drummond, 1990). Importantly, the granites show high Sr (average 374 ppm) abundances and high Sr/Y (average 35.5) and (La/Yb)_N (average 33.4) ratios, with low Y (average 10.3 ppm) and Yb (average 0.83 ppm) contents. These features suggest a geochemical affinity to adakites (Fig. 10). Nevertheless, the absence of mantle-derived components implies that formation of the studied granites was unlikely partial melts of subducted oceanic slabs interacted with peridotite (Martin et al., 2005). Therefore, their adakite-like characteristics were probably related to the fractionated REE patterns and negligible Eu anomalies (Fig. 4), and still indicate considerable residual garnet and hornblende without plagioclase in the source (Rapp and Watson, 1995). In addition, the negative correlations between TiO₂, Fe₂O₃^T, P₂O₅, Zr and SiO₂ were possibly associated with fractionation of accessory minerals, such as Ti- and Fe-bearing phases (e.g., ilmenite), apatite and zircon. In summary, we advocate that the Wenjiaping and Wulaxi granites were most likely produced by partial melting of crustal melts and subsequent fractional crystallization. This viewpoint corroborates previous petrogenetic model of I-type granites (e.g., Turpin et al., 1990; Barbarin, 1996; Chappell et al., 2012).

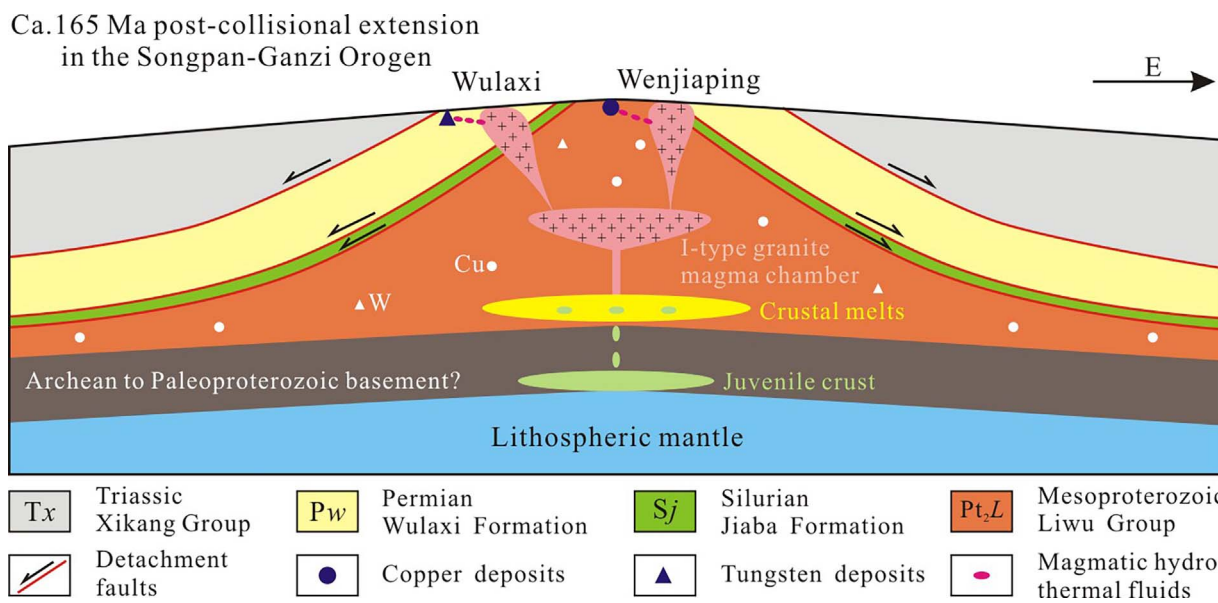


Fig. 12. Schematic diagram showing petrogenetic model for the Wenjiaping and Wulaxi granites in the Jianglang dome.

5.5. Tectonic and metallogenetic implications

Based on the discovery of numerous ductile normal faults, Xu et al. (1992) proposed that the extensional regime was predominant at ca. 160 Ma in the SGO. Chronological studies have indicated that partial melting of the overthickened orogenic crust produced *syn-collisional* granitic intrusions with ages of 220–200 Ma (Roger et al., 2004, 2010; Zhang et al., 2006, 2007; Xiao et al., 2007; Weislogel, 2008), and post-collisional granites with ages of 200–150 Ma (Roger et al., 2004; Reid et al., 2007). In this paper, zircon U-Pb chronology suggests emplacement ages of 164.8–163.4 Ma (Fig. 5) for the Wenjiaping and Wulaxi granite plutons. These ages indicate a post-collisional extensional affinity, which is supported by the Rb-(Y + Nb) tectonic discrimination diagram (Fig. 11). We thus point out that two granites were products of decompression melting of continental crust associated with ca. 165 Ma post-collisional extension in the SGO (Fig. 12).

Prior studies have classified the Jianglang dome as a metamorphic core complex (Yan et al., 1997, 2003), with detachment faults between the tectonostratigraphic units (Fig. 1). This indicates that the doming process and two studied post-collisional granites were both related to lithospheric extension. However, two plutons intrude the Jianglang dome (Fig. 1) and the granites are undeformed (Fig. 2), implying a doming age earlier than ca. 165 Ma. Yan et al. (2003) pointed out that the Triassic strata, in ductile fault contact with the Permian, were involved in the formation of the Jianglang dome. This geological feature suggests that the doming was posterior to the Triassic and thus during the Early to Middle Jurassic. The viewpoint is further illuminated by K-Ar age of 177 Ma for illite within mylonitic foliation from the Xikang Group (SBGMR, 1991). In addition, according to SHRIMP U-Pb dating, gneissic complex in the Gongcai dome (Fig. 1a) has zircons with metamorphic age of 177 ± 3 Ma ($n = 7$, Zhou et al., 2002). This metamorphism was associated with the exhumation of this dome and the beginning of nearly east-west extensional deformation (Zhou et al., 2002). Therefore, we conclude that tectonic domes in the eastern margin of the SGO were most likely formed in a uniform geodynamic (i.e., post-collisional) process (Xu et al., 1992; Yan et al., 1997).

Previous silicon, sulfur and lead isotopic systematics revealed that the ore-forming elements of polymetallic deposits in the Jianglang dome were derived from the Mesoproterozoic Liwu Group, which has relatively high Cu and W abundances (Yan et al., 1997; Yao et al., 2008). Significantly, the metal sulfides (including chalcopyrite, pyrrhotite, sphalerite, galena and pyrite) have $\delta^{34}\text{S}$ values of 7.5–1.5‰ (Yan et al., 1997; Chen et al., 2011), which are consistent with those of granitoid rocks ($1.0 \pm 6.1\text{‰}$, Seal, 2006). The boron isotopic data of ore-associated tourmalines ($\delta^{11}\text{B} = -15.47 \pm 0.83\text{‰}$ to $-5.91 \pm 0.67\text{‰}$) also indicated a magmatic hydrothermal affinity (Zhou et al., 2017). Recently, Li et al. (2016) obtained a molybdenite Re-Os isochron age of 163.7 ± 1.9 Ma ($n = 6$, MSWD = 0.42) for the skarn tungsten deposits to the south of the Wulaxi pluton. Chalcopyrite Re-Os dating indicates an isochron age of 151.1 ± 4.8 Ma for the Liwu and Zhongzui high-grade Cu-sulfide stratiform deposits (Zhou et al., 2017). These data are close to the emplacement ages (164.5–163.4 Ma) of the granite plutons, and provide robust chronological constraints on a magmatic hydrothermal affinity for these Cu-W deposits. Therefore, we advocate that the 164.5–163.4 Ma granitic magmas mobilized the ore-forming materials within the Liwu Group and further formed hydrothermal Cu-W deposits in the Jianglang dome (Fig. 12). As mentioned above, extensional tectonic domes in the eastern margin of the SGO should be associated with uniform geodynamic setting (Xu et al., 1992; Yan et al., 1997), which provides promising exploration potential for ca. 165 Ma hydrothermal deposits in this region.

6. Conclusions

Zircon U-Pb chronology yields emplacement ages of ca. 164.5–163.4 Ma for the Wenjiaping and Wulaxi granite plutons. This

indicates a magmatic hydrothermal affinity for the 163.7–151.1 Ma Cu-W deposits in the Jianglang dome. Integration of petrographic and geochemical data shows that two granites are most likely I-type that formed in a post-collisional extensional setting. They were derived from remelting of ancient continental crust with minor juvenile crust, and possibly underwent extensive fractional crystallization. Combined with prior studies, it is suggested that the doming of the Jianglang dome occurred during the Early to Middle Jurassic.

Acknowledgments

This work was financially supported by Young Scholars Development Fund of Southwest Petroleum University (No. 201499010083), Scientific Research Starting Project of Southwest Petroleum University (No. 2015QHZ009) and Scientific Research Project of Education Department of Sichuan Province (No. 15ZB0058). We are grateful to two anonymous reviewers and editor Tomas Magna for their insightful comments and many important corrections in English.

References

- Altherr, R., Siebel, W., 2002. I-type plutonism in a continental back-arc setting: miocene granitoids and monzonites from the central Aegean Sea, Greece. *Contrib. Mineral. Petrol.* 143, 397–415.
- Barbarin, B., 1996. Genesis of the two main types of peraluminous granitoids. *Geology* 24, 295–298.
- Barth, M.G., McDonough, W.F., Rudnick, R.L., 2000. Tracking the budget of Nb and Ta in the continental crust. *Chem. Geol.* 165, 197–213.
- Boehnke, P., Watson, E.B., Trail, D., Harrison, T.M., Schmitt, A.K., 2013. Zircon saturation re-revisited. *Chem. Geol.* 351, 324–334.
- Castro, A., Moreno-Ventas, I., De la Rosa, J.D., 1991. H-type (hybrid) granitoids: a proposed revision of the granite-type classification and nomenclature. *Earth Sci. Rev.* 31, 237–253.
- Cawthorn, R.G., Brown, P.A., 1976. A model for the formation and crystallization of corundum-normative calc-alkaline magmas through amphibole fractionation. *J. Geol.* 84, 467–476.
- Chappell, B.W., White, A.J.R., 1974. Two contrasting granite types. *Pacific Geol.* 8, 173–174.
- Chappell, B.W., Bryant, C.J., Wyborn, D., 2012. Peraluminous I-type granites. *Lithos* 153, 142–153.
- Chappell, B.W., 1999. Aluminium saturation in I- and S-type granites and the characterization of fractionated haplogranites. *Lithos* 46, 535–551.
- Chen, M.H., Ding, J., Chen, D.Q., 2011. Origin of the ore-forming matter from the Liwu copper orefield in Jiulong, Sichuan. *Sediment. Geol. Tethyan Geol.* 31, 89–93 (in Chinese with English abstract).
- Chen, Q., Sun, M., Long, X.P., Zhao, G.C., Yuan, C., 2016. U-Pb ages and Hf isotopic records of detrital zircons from the late Neoproterozoic and Silurian-Devonian sedimentary rocks of the western Yangtze Block: implications for its tectonic evolution and continental affinity. *Gondwana Res.* 31, 184–199.
- Collins, W.J., Beams, S.D., White, A.J.R., Chappell, B.W., 1982. Nature and origin of A-type granites with particular reference to southeastern Australia. *Contrib. Mineral. Petrol.* 80, 189–200.
- Dai, Y.P., Zhang, L.C., Zhu, M.T., Wang, C.L., Liu, L., Xiang, P., 2014. The composition and genesis of the Mesoarchean Dagushan banded iron formation (BIF) in the Anshan area of the North China Craton. *Ore Geol. Rev.* 63, 353–373.
- Dai, Y.P., Zhang, H.H., Zhu, Y.D., Shen, Z.W., Li, T.Z., Ma, D., 2016. Review on Jianglang dome and Liwu-type copper deposit in the western margin of Yangtze block. *J. Earth Sci. Environ.* 38, 66–78 (in Chinese with English abstract).
- Dall'Agnol, R., Scaillet, B., Pichavant, M., 1999. An experimental study of a lower proterozoic A-type granite from the eastern Amazonian craton, Brazil. *J. Petrol.* 40, 1673–1698.
- Defant, M.J., Drummond, M.S., 1990. Derivation of some modern arc magmas by melting of young subducted lithosphere. *Nature* 347, 662–665.
- Eby, G.N., 1992. Chemical subdivision of the A-type granitoids: petrogenetic and tectonic implications. *Geology* 20, 641–644.
- Feng, X.L., Liu, Y.S., Zhang, H.H., Wu, Z.B., Li, T.Z., 2008. Quartz inclusions from the ore-bearing rocks in the Liwu copper deposit, Jiulong, Sichuan. *Sediment. Geol. Tethyan Geol.* 28, 1–11 (in Chinese with English abstract).
- Geng, H.Y., Sun, M., Yuan, C., Xiao, W.J., Xian, W.S., Zhao, G.C., Zhang, L.F., Wong, K., Wu, F.Y., 2009. Geochemical, Sr-Nd and zircon U-Pb-Hf isotopic studies of late carboniferous magmatism in the west Junggar, Xinjiang: implications for ridge subduction? *Chem. Geol.* 266, 373–398.
- Harrowfield, M.J., Wilson, J.L., 2005. Indosian deformation of the Songpan Garze fold belt, northeast Tibetan plateau. *J. Struct. Geol.* 27, 101–117.
- Hoskin, P.W.O., Schaltegger, U., 2003. The composition of zircon and igneous and metamorphic petrogenesis. *Rev. Mineral. Geochem.* 53, 27–62.
- Irvine, T., Baragar, W., 1971. A guide to the chemical classification of the common volcanic rocks. *Can. J. Earth Sci.* 8, 523–548.

- Jackson, S.E., Pearson, N.J., Griffin, W.L., Belousova, E.A., 2004. The application of laser ablation-inductively coupled plasma-mass spectrometry to *in situ* U-Pb zircon geochronology. *Chem. Geol.* 211, 47–69.
- King, P.L., White, A.J.R., Chappell, B.W., Allen, C.M., 1997. Characterization and origin of aluminous A-type granites from the Lachlan fold belt, southeastern Australia. *J. Petrol.* 38, 371–391.
- Le Maitre, R.W., 1989. A Classification of Igneous Rocks and Glossary of Terms. Oxford, Blackwell, pp. 1–193.
- Li, Z.X., Bogdanova, S.V., Collins, A.S., Davidson, A., Waele, B.D., Ernst, R.E., Fitzsimons, I.C.W., Fuck, R.A., Gladkochub, D.P., Jacobs, J., Karlstrom, K.E., Lu, S., Natapov, L.M., Pease, V., Pisarevsky, S.A., Thrane, K., Vernikovsky, V., 2008. Assembly, configuration, and break-up history of Rodinia: a synthesis. *Precambrian Res.* 160, 179–210.
- Li, T.Z., Feng, X.L., Zhang, H.H., Tang, G.L., Wu, Z.B., Xia, X.B., 2010. Geochemical characteristics of the ore-bearing rock series and genesis of the Liwu copper deposit, Sichuan Province. *Geol. Explor.* 46, 921–930 (in Chinese with English abstract).
- Li, T.Z., Zhou, Q., Zhang, H.H., Dai, Y.P., Ma, G.T., Ma, D., Shen, Z.W., 2016. Ore geology and molybdenite Re-Os dating of the Wulaxi tungsten deposit in western Sichuan. *Geol. J. China Univ.* 22, 423–430 (in Chinese with English abstract).
- Li, Y.S., Gao, S., Hu, Z.C., Gao, C.G., Zong, K.Q., Wang, D.B., 2010. Continental and oceanic crust recycling-induced melt-peridotite interactions in the trans-north China orogen: U-Pb dating, Hf isotopes and trace elements in zircons from mantle xenoliths. *J. Petrol.* 51, 537–571.
- Maniar, P.D., Piccoli, P.M., 1989. Tectonic discrimination of granitoids. *Geol. Soc. Am. Bull.* 101, 635–643.
- Martin, H., 1986. Effect of steeper Archean geothermal gradient on geochemistry of subduction-zone magmas. *Geology* 14, 753–756.
- Martin, H., Smithies, R.H., Moyen, J.F., Champion, D., 2005. An overview of adakite, tonalite-trondjemite-granodiorite (TTG), and sanukitoid: relationships and some implications for crust evolution. *Lithos* 79, 1–24.
- Middlemost, E.A.K., 1994. Naming materials in the magma/igneous rock system. *Earth Sci. Rev.* 37, 215–224.
- Pearce, J.A., Harris, N.B.W., Tindle, A.G., 1984. Trace element discrimination diagrams for the tectonic interpretation of granitic rocks. *J. Geol.* 25, 956–983.
- Pecceirillo, A., Taylor, S.R., 1976. Geochemistry of Eocene calc-alkaline volcanic rocks from the Kastamonu area, Northern Turkey. *Contrib. Tominal. Petrol.* 58, 63–81.
- Polat, A., Hofmann, A.W., Rosing, M.T., 2002. Boninite-like volcanic rocks in the 3.7–3.8 Ga Isua greenstone belt: west Greenland; geochemical evidence for intra-oceanic subduction zone processes in the early Earth. *Chem. Geol.* 184, 231–254.
- Rapp, R.P., Watson, E.B., 1995. Dehydration melting of metabasalt at 8–32 kbar: implications for continental growth and crust-mantle recycling. *J. Petrol.* 36, 891–931.
- Reid, A., Wilson, C.J.L., Shun, L., Pearson, N., Belousova, E., 2007. Mesozoic plutons of the Yidun arc, SW China: u/Pb geochronology and Hf isotopic signature. *Ore Geol. Rev.* 34, 88–106.
- Roger, F., Malavieille, J., Leloup Ph.D. Calassou, S., Xu, Z., 2004. Timing of granite emplacement and cooling in the Songpan-Garze (eastern Tibetan Plateau) with tectonic implications. *J. Asian Earth Sci.* 22, 465–481.
- Roger, F., Jolivet, M., Malavieille, J., 2010. The tectonic evolution of the Songpan-Garze (North Tibet) and adjacent areas from Proterozoic to Present: a synthesis. *J. Asian Earth Sci.* 39, 254–269.
- SBGMR (Sichuan Bureau of Geology and Mineral Resources), 1991. Regional Geology of Sichuan Province. Geological Publishing House, Beijing, pp. 1–680 (in Chinese).
- Seal, R.R., 2006. Sulfur isotope geochemistry of sulfide minerals. *Rev. Mineral. Geochem.* 61, 633–677.
- Sláma, J., Košler, J., Condon, D.J., Crowley, J.L., Gerdes, A., Hanchar, J.M., Horstwood, M.S.A., Morris, G.A., Nasdala, L., Norberg, N., Schaltegger, U., Schoene, B., Tubrett, M.N., Whitehouse, M.J., 2008. Plešovice zircon: a new natural reference material for U-Pb and Hf isotopic microanalysis. *Chem. Geol.* 249, 1–35.
- Sun, S.S., McDonough, W.F., 1989. Chemical and Isotopic Systematics of Oceanic Basalts: Implications for Mantle Composition and Processes 42. Geological Society London, Special Publications, pp. 313–345.
- Sun, J.P., Chen, S.Y., Liu, C.L., Ma, Y.S., Yin, C.M., Peng, Y., Shao, P.C., Ma, S., Liu, J., 2016. Tectonic setting of Northeastern Qaidam Basin and its evolution during the Late Paleozoic: evidence from geochemical characteristics of detrital rock. *Earth Sci. Front.* 23, 45–55 (in Chinese with English abstract).
- Taylor, S.R., McLennan, S.M., 1985. The Continental Crust: Its Composition and Evolution. Blackwell Oxford, pp. 1–328.
- Tchameni, R., Mezger, K., Nsifa, N.E., Pouclet, A., 2001. Crustal origin of early proterozoic syenites in the Congo craton (Ntem complex), south Cameroon. *Lithos* 57, 23–42.
- Turpin, L., Cuney, M., Friedrich, M., Bouchez, J.L., Aubertin, M., 1990. Metagneous origin of Hercynian peraluminous granites in N.W. French Massif Central: implications for crustal history reconstructions. *Contrib. Mineral. Petrol.* 104, 163–172.
- Warren, I., Simmons, S.F., Mauk, J.L., 2007. Whole-rock geochemical techniques for evaluating hydrothermal alteration, mass changes, and compositional gradients associated with epithermal Au-Ag mineralization. *Econ. Geol.* 102, 923–948.
- Watson, E.B., Harrison, T.M., 1983. Zircon saturation revisited: temperature and composition effects in a variety of crustal magma types. *Earth Planet. Sci. Lett.* 64, 295–304.
- Weislogel, A.L., Graham, S.A., Chang, E.Z., Wooden, J.L., Gehrels, G.E., Yang, H., 2006. Detrital zircon provenance of the Late Triassic Songpan-Garze complex: sedimentary record of collision of the North and South China blocks. *Geology* 34, 97–100.
- Weislogel, A.L., 2008. Tectonostratigraphic and geochronologic constraints on evolution of the northeast Paleotethys from the Songpan-Ganzi complex, central China. *Tectonophysics* 451, 331–345.
- Whalen, J.B., Currie, K.L., Chappell, B.W., 1987. A-type granites: geochemical characteristics, discrimination and petrogenesis. *Contrib. Mineral. Petrol.* 95, 407–419.
- Wiedenbeck, M., Alle, P., Corfu, F., Griffin, W.L., Meier, M., Oberli, F., Von Quadt, A., Roddick, J.C., Spiegel, W., 1995. Three natural zircon standards for U-Th-Pb, Lu-Hf, trace element and REE analyses. *Geostand. Geoanal. Res.* 19, 1–23.
- Woodhead, J.D., Hergt, J.M., 2005. A preliminary appraisal of seven natural zircon reference materials for *in situ* Hf isotope determination. *Geostand. Geoanal. Res.* 29, 183–195.
- Wyborn, D., Turner, B.S., Chappell, B.W., 1987. The Boggy Plain Supersuite: a distinctive belt of I-type igneous rocks of potential economic significance in the Lachlan Fold Belt. *Aust. J. Earth Sci.* 34, 21–43.
- Xiao, L., Xu, Y.G., Mei, H.J., Zheng, Y.F., He, B., Pirajno, F., 2004. Distinct mantle sources of low-Ti and high-Ti basalts from the western Emeishan large igneous province, SW China: implications for plume-lithosphere interaction. *Earth Planet. Sci. Lett.* 228, 525–546.
- Xiao, L., Zhang, H.F., Clemens, J.D., Wang, Q.W., Kan, Z.Z., Wang, K.M., Ni, P.Z., Liu, X.M., 2007. Late Triassic Granitoids of the Eastern Margin of the Tibetan Plateau: geochronology, petrogenesis and implications for tectonic evolution. *Lithos* 96, 436–452.
- Xu, Z.Q., Hou, L.W., Wang, Z.X., Fu, X.F., Huang, M.H., 1992. Orogenic Processes of the Songpan-Garze Belt of China. Geological Publishing House, Beijing, pp. 1–190 (in Chinese).
- Yan, D.P., Song, H.L., Fu, Z.R., Tian, J.Y., 1997. Metamorphic Core Complexes in the Western Margin of the Yangtze Platform. Geological Publisher House, Beijing, pp. 1–94 (in Chinese with English abstract).
- Yan, D.P., Zhou, M.F., Song, H.L., Fu, Z.R., 2003. Structural style and tectonic significance of the Jianglang dome in the eastern margin of the Tibetan Plateau, China. *J. Struct. Geol.* 25, 765–779.
- Yao, P., Wang, M.J., Li, J.Z., Ma, G.T., Zhu, X.P., 2008. Isotopic tracing of the Liwu-type Cu-rich deposits and its ore-forming geological significance. *Acta Geoscientica Sinica* 29, 691–696 (in Chinese with English abstract).
- Yuan, C., Zhou, M.F., Sun, M., Zhao, Y.J., Wilde, S., Long, X.P., Yan, D.P., 2010. Triassic granitoids in the eastern Songpan-Ganzi Fold Belt, SW China: magmatic response to geodynamics of the deep lithosphere. *Earth Planet. Sci. Lett.* 290, 481–492.
- Zhang, H.F., Zhang, L., Harris, N., Jin, L., Yuan, H.L., 2006. U-Pb zircon ages, geochemical and isotopic compositions of granitoids in Songpan-Ganzi fold belt, eastern Tibetan Plateau: constraints on petrogenesis and tectonic evolution of the basement. *Contrib. Mineral. Petrol.* 152, 75–88.
- Zhang, H.F., Parrish, R., Zhang, L., Xu, W.C., Yuan, H.L., Gao, S., Crowley, Q.G., 2007. A-type granite and adakitic magmatism association in Songpan-Garze fold belt, eastern Tibetan Plateau: implication for lithospheric delamination. *Lithos* 97, 323–335.
- Zhou, M.F., Yan, D.P., Kennedy, A.K., Li, Y.Q., Ding, J., 2002. SHRIMP U-Pb zircon geochronological and geochemical evidence for Neoproterozoic arc-magmatism along the western margin of the Yangtze Block, South China. *Earth Planet. Sci. Lett.* 196, 51–67.
- Zhou, Q., Li, W.C., Zhang, H.H., Li, T.Z., Yuan, H.Y., Feng, X.L., Li, C., Liao, Z.W., Wang, S.W., 2017. Post-magmatic hydrothermal origin of late Jurassic Liwu copper polymetallic deposits, western China: direct chalcopyrite Re-Os dating and Pb-B isotopic constraints. *Ore Geol. Rev.* 89, 526–543.